

The Zwicky Transient Facility Catalog of Periodic Variable Stars

XIAODIAN CHEN,¹ SHU WANG,¹ LICAI DENG,¹ RICHARD DE GRIJS,^{2,3,4} MING YANG,⁵ AND HAO TIAN⁶

¹CAS Key Laboratory of Optical Astronomy, National Astronomical Observatories, Chinese Academy of Sciences, Beijing 100101, China

²Department of Physics and Astronomy, Macquarie University, Balaclava Road, Sydney, NSW 2109, Australia

³Research Centre for Astronomy, Astrophysics and Astrophotonics, Macquarie University, Balaclava Road, Sydney, NSW 2109, Australia

⁴International Space Science Institute–Beijing, 1 Nanertiao, Zhongguancun, Hai Dian District, Beijing 100190, China

⁵IAASARS, National Observatory of Athens, Vas. Pavlou & I. Metaxa, Penteli 15236, Greece

⁶Key Laboratory of Space Astronomy and Technology, National Astronomical Observatories, Chinese Academy of Sciences, Beijing 100101, China

(Received 2019 November 29; Revised 2020 May 18; Accepted 2020 Jun 11)

Submitted to ApJS

ABSTRACT

The number of known periodic variables has grown rapidly in recent years. Thanks to its large field of view and faint limiting magnitude, the Zwicky Transient Facility (ZTF) offers a unique opportunity to detect variable stars in the northern sky. Here, we exploit ZTF Data Release 2 (DR2) to search for and classify variables down to $r \sim 20.6$ mag. We classify 781,602 periodic variables into 11 main types using an improved classification method. Comparison with previously published catalogs shows that 621,702 objects (79.5%) are newly discovered or newly classified, including ~ 700 Cepheids, ~ 5000 RR Lyrae stars, $\sim 15,000$ δ Scuti variables, $\sim 350,000$ eclipsing binaries, $\sim 100,000$ long-period variables, and about 150,000 rotational variables. The typical misclassification rate and period accuracy are on the order of 2% and 99%, respectively. 74% of our variables are located at Galactic latitudes, $|b| < 10^\circ$. This large sample of Cepheids, RR Lyrae, δ Scuti stars, and contact (EW-type) eclipsing binaries is helpful to investigate the Galaxy's disk structure and evolution with an improved completeness, areal coverage, and age resolution. Specifically, the northern warp and the disk's edge at distances of 15–20 kpc are significantly better covered than previously. Among rotational variables, RS Canum Venaticorum and BY Draconis-type variables can be separated easily. Our knowledge of stellar chromospheric activity would benefit greatly from a statistical analysis of these types of variables.

Keywords: Periodic variable stars (1213); Distance indicators (394); Cepheid variable stars (218); RR Lyrae variable stars (1410); Galaxy disks (589); Eclipsing binary stars (444); Long period variable stars (935)

1. INTRODUCTION

Periodic or quasi-periodic variables encompass mainly eclipsing binary systems and rotational stars characterized by extrinsic variability, while pulsating variables are among objects exhibiting intrinsic fluctuations in the variability tree (Gaia Collaboration et al. 2019). These objects are interesting, since their periods contain information about their luminosity or mass. Variable

stars have been studied for several hundred years. However, this field has been advancing significantly in recent years. With increases in the depth and efficacy of time-domain surveys, the number of newly detected variables is roughly doubled every year. *Gaia*'s third Data Release (DR3) is expected to include 7 million variables, with about one-third to half of periodic nature. This huge number is of the same order as the number of extant stellar spectra. By combining the spectra and light curves (LCs) of variable stars, we will be able to improve our knowledge of a range of fundamental stellar parameters, which in turn can benefit developments in theory and the applications of stellar physics. A com-

plete catalog of all-sky periodic variables can also be used to separate variable and non-variable stars in spectroscopic surveys—such as those undertaken with the Large Sky Area Multi-Object Fiber Spectroscopic Telescope (LAMOST; Cui et al. 2012; Deng et al. 2012) and the Sloan Digital Sky Survey (SDSS; Eisenstein et al. 2011)—to reduce the systematic effects pertaining to the presence of variables.

Although searches for variables date back hundreds of years, the number of known variables first increased significantly in the 1990s thanks to the development of CCDs. The Massive Compact Halo Object (MACHO) survey (Alcock et al. 1993) found 20,000 variable stars in the Large Magellanic Cloud (LMC). The Optical Gravitational Lensing Experiment (OGLE) subsequently made significant progress in this field. Over its 20-year duration, OGLE detected more than 900,000 variables in the Magellanic Clouds, the Galactic bulge, and the Galactic plane (Udalski et al. 1992, 2015). The first all-sky variability survey was carried out by the All Sky Automated Survey (ASAS), which detected 10,000 eclipsing binaries and 8000 periodic pulsating stars (Pojmanski et al. 2005). Several thousand variables were also found by the Robotic Optical Transient Search Experiment (ROTSE; Akerlof et al. 2000) and the Lincoln Near-Earth Asteroid Research (Palaversa et al. 2013, LINEAR) project. The Catalina Surveys (Drake et al. 2014, 2017) found more than 100,000 variables, covering almost the entire sky, which allowed significant progress to be made in studying streams, structures, and the shape of the Milky Way’s halo. Variable surveys have also been undertaken in infrared passbands, e.g., the VISTA Variables in the Vía Láctea (VVV) survey (Minniti et al. 2010) and the VISTA survey of the Magellanic Clouds system (VMC; Cioni et al. 2011). In 2018, a number of variable-star catalogs were published, including the All-Sky Automated Survey for Supernovae (ASAS-SN; Jayasinghe et al. 2018), the Asteroid Terrestrial-impact Last Alert System (ATLAS; Heinze et al. 2018), the Wide-field Infrared Survey Explorer (WISE) catalog of periodic variable stars (Chen et al. 2018b), and the variable catalog of *Gaia* DR2 (Clementini et al. 2019; Mowlavi et al. 2018). The number of known variables is currently experiencing a second substantial increase, resulting in millions of known variable objects.

Alongside the increasing numbers of known variables, advances have also been made as regards the corresponding and ancillary science, e.g., pertaining to distance measurements, structure analysis, stellar-mass black hole searches, and multi-messenger astrophysics. As regards distance indicators, detached eclipsing bina-

ries were used to measure the distance to the LMC to an accuracy of 1% (Pietrzyński et al. 2019). This accurate benchmark distance is of great importance to refine the value of the Hubble parameter (Riess et al. 2019). As to structure analyses, the sample of newly found classical Cepheids led to the first intuitive 3D map of two-thirds of the Milky Way’s disk (Chen et al. 2019; Skowron et al. 2019a). This new map will help us understand the evolution of both the Galaxy’s spiral arms and its outer disk. As regards long-period binary variables, their unseen companions may include black holes. A low-mass black hole has been found to orbit a giant star with an orbital period of ~ 83 days (Thompson et al. 2019). Searching for variables with the shortest or the longest periods is attractive (Burdge et al. 2019; Graham et al. 2015), since such systems contain information about both the properties of their electromagnetic radiation and possible gravitational-wave signals that can motivate multi-messenger astrophysics.

In this paper, we search for periodic variables in the recent data release of the Zwicky Transient Facility (ZTF), the deepest time-domain survey of the northern sky. Periodicities are analyzed for the full database to identify a sample of periodic variables that is as complete as possible. Using an improved method of classification, 781,602 variables belonging to 11 main types are classified. Our sample’s detection rate of newly identified objects is about 80%. We construct a large variable-star catalog that will benefit many follow-up studies. The data are described in Section 2. We explain how we identify and classify variables in Sections 3 and 4, respectively. The new variable catalog and a comparison of its consistency with previous catalogs are covered in Section 5. We provide a detailed discussion of each type of variable object and their applications in Section 6. Section 7 summarizes our conclusions.

2. ZTF DATA

The ZTF is a 48-inch Schmidt telescope with a 47 deg² field of view (Masci et al. 2019; Bellm et al. 2019). This large field of view ensures that the ZTF can scan the entire northern sky every night. The ZTF survey started on 2018 March 17. During the planned three-year survey, ZTF is expected to acquire ~ 450 observational epochs for 1.8 billion objects. Its main science aims are the physics of transient objects, stellar variability, and solar system science (Graham et al. 2019; Mahabal et al. 2019). ZTF DR2 contains data acquired between 2018 March and 2019 June, covering a timespan of around 470 days. ZTF DR2 photometry is obtained in two observation modes, three-night cadence for the northern sky and one-night cadence for the Galactic

plane, $|b| \leq 7^\circ$, Dec. $> -25^\circ$. The photometry is provided in the g and r bands, with a uniform exposure time of 30 s per observation. The limiting magnitude is $r \sim 20.6$ mag. ZTF g and r photometry is calibrated with the help of Pan-STARRS1 DR1 (Chambers et al. 2016); there is only a small offset of ~ 0.01 mag between both systems at the bright end ($r < 15.5$ mag). ZTF DR2 includes more than 1 billion stars, about half of which have > 20 epochs of observations. For the majority of stars located in the northern Galactic plane, ZTF contains ~ 150 epochs of observations. As such, ZTF can be used to detect numerous variables in the northern Galactic plane, which has not been well-studied by previous time-domain surveys. We downloaded the full catalog (comprising a total volume of ~ 3.4 TB),¹ which is provided in the form of 856 files, ordered as a function of spatial position.

3. SEARCH FOR PERIODIC VARIABLES

To search for periodic variables, we need to impose some conditions to make the process easier and quicker. First, we only selected objects in the ZTF data with at least 20 detections. Adoption of this criterion will not cause us to miss many periodic candidates, since a period’s false-alarm probability (FAP) based on < 20 detections is high. Second, poor-quality images and photometry were excluded by adopting INFOBITS $< 33, 554, 432$ and catflags $\neq 32, 768$, respectively. Third, preliminary searching for periodicity for a given object was based on photometry associated with the same internal product ID. This choice made this process much quicker. Although a fraction of the objects have multiple internal IDs, since they may have been observed for different projects, their periodicity is unlikely to be missed based on analysis of the data from the main project. A redetermination of the period will be done based on the object’s position (R.A. and Dec.) during the next steps.

We cut the data into smaller segments to mitigate computational memory restrictions and ran Lomb–Scargle periodogram (Lomb 1976; Scargle 1982) analysis using the MATLAB code ‘plomb’ to search for variables. The code returns the Lomb–Scargle power spectral density (PSD) based on the maximum input frequency. We searched for periods from 0.025 to 1000 days (in steps of 0.0001 day^{-1} in frequency), a range covering variables from short-period δ Scuti to long-period Mira stars. We attempted to exclude aliased periods—such as one day and its multiples—using a method similar to that of Jayasinghe et al. (2019b). Some aliased periods were

successfully excluded, although many remained. Many candidate variables with aliased periods are real long-period variables (LPVs). Their aliased periods are a combination of real periods, P_r , and the one-day sampling cadence, P_c : $1/P_a = 1/P_r + 1/P_c$, $P_c = 0.5, 1, 2, \dots$. After excluding P_a , the real periods of well-sampled variables could be obtained (see also Section 5.3).

A number of parameters were recorded during this process to help with the selection of variable candidates, including the FAP, which represents the confidence of the periodicity determination. We selected periodic candidates by imposing $\text{FAP} < 0.001$. Adoption of this criterion mistakenly excludes only a few short-period variables. These will be rediscovered with better sampling in the ZTF’s future DRs. Other parameters of importance are the mean PSD, $\langle P_f \rangle$, and the number of frequencies associated with $\text{PSD} > 0.5\text{PSD}_{\text{max}}$. These parameters are used to avoid inclusion of false variables produced by abnormal sampling. ZTF is not affected by problems caused by the inhomogeneous distribution of the data points, except for LPVs. Therefore, we do not need to record any parameters to trace the distribution of the data points in the phase-folded LC. Periodicities were determined in both the g and r bands, and candidates were accepted if the LC in one band met all conditions.

Running the code took one month on two computers with a total of 18 i7 CPUs. A grand total of 1.4 million variable candidates were recorded. We redetermined their periods based on all of the photometric data within $1''$ around their spatial position. The LCs were fitted with a fourth-order Fourier function, $f = a_0 + \sum_{i=1}^4 a_i \cos(2\pi it/P + \phi_i)$, which is a suitable choice for survey LCs to avoid missing important parameters or overfitting. About 90% of these ZTF LCs have a_4 values less than the typical photometric uncertainties of 0.02 mag. a_i and ϕ_i denote amplitudes and phases for each order, respectively. Candidates with poorly fitted LCs were excluded using the adjusted R^2 (which represents how well LCs are fitted by the Fourier function), i.e., $R_g^2 < 0.4$ and $R_r^2 < 0.4$. Objects still characterized by aliased periods were excluded based on their distributions in the period versus R^2 or ϕ_{21} ($\phi_{21} = \phi_2 - 2\phi_1$) diagram, e.g., objects with $|P - 1| < 0.03$ days and $R^2 < 0.8$ or $|\phi_{21,r} - \phi_{21,g}| > 0.2$ were excluded. At this point, 1 million candidates remained for further classification.

4. CLASSIFICATION

Classification is more challenging than the identification process. The main idea is based on the varying densities of different variables in multi-dimensional space.

¹ https://irsa.ipac.caltech.edu/data/ZTF/lc_dr2/

Parameters including the period ($\log P$), phase difference (ϕ_{21}), amplitude ratio ($R_{21} = a_2/a_1$), amplitude (Amp.), absolute Wesenheit magnitude ($M_{W_{gr}}$), and adjusted R^2 were adopted to help with our classification. The period is the most significant parameter; ϕ_{21} , R_{21} , and Amp. are parameters determined from the LC fits. The absolute Wesenheit magnitude is used to separate the variables in the overlap region of the LCs' parameter space. It is also helpful to narrow down the types of low-amplitude variables. To avoid significant extinction in the optical bands, we calculated Wesenheit magnitudes, $m_{W_{gr}} = \langle g \rangle - R_{gr} \times (\langle g \rangle - \langle r \rangle)$, making use of the g, r photometry. Here, $\langle g \rangle$ and $\langle r \rangle$ are the mean magnitudes determined from our LC fits. We adopted the recently derived Galactic extinction law (Wang & Chen 2019) based on red clump stars with accurate parameters and obtained $m_{W_{gr}} = 3.712\langle r \rangle - 2.712\langle g \rangle$.

Gaia DR2 parallaxes (Gaia Collaboration et al. 2018) were adopted to estimate the absolute magnitudes. Since many of our objects are located in the Galactic plane, we used the inverse of the parallaxes to estimate distances. To reduce the systematic effects of the Lutz–Kelker bias (Lutz & Kelker 1973), only parallaxes with $\varpi > 0.2$, $\sigma_\varpi/\varpi < 0.2$ and $\sigma_\varpi/\varpi < 0.5$ were adopted for our detailed classification and the dwarf–giant separation, respectively. R^2 contains information to separate characteristic and non-characteristic LCs, where ‘characteristic’ LCs have similar patterns, and we can find a rule to classify variable stars based on their LCs. ‘Non-characteristic’ LCs exhibit arbitrary patterns. In other words, variables with characteristic LCs form either a clump or a sequence in the P versus ϕ_{21} diagram, while variables with non-characteristic LC exhibit a random distribution. As R^2 decreases, the probability of variables with characteristic LCs—e.g., eclipsing binaries and radially pulsating stars—decreases.

Note that the relation between the amplitudes in both filters ($\text{Amp}_g = a \times \text{Amp}_r + b$) is different for each variable. The 1σ scatter (0.03–0.06 mag) on these relations in the current database is too large to allow for a robust classification of the majority of our variables, considering that the amplitude difference between the g and r bands is not significant. As such, we did not adopt this criterion for automatic classification, but only for a visual check of the easily-confused variables.

The classification process proceeded based on the auto-manual Density-Based Spatial Clustering of Applications with Noise (DBSCAN). DBSCAN clusters data points based on a neighborhood search radius and a minimum number of neighbors. Both of these parameters were adjusted in each step to achieve an optimal separation of the different variables. Since classi-

fication rules for variables (in particular for variables with non-characteristic LCs) are not well-established, we only classified variables with a significant density in parameter space. The classification order progresses from Cepheids, to fundamental-mode (RRab) and first-overtone (RRc) Lyrae, δ Scuti stars, eclipsing binaries, and finally to variables with non-characteristic LCs.

As our first step, we established the best samples of Cepheids, RRab and RRc Lyrae, and δ Scuti stars based on strict constraints on the LC quality ($R^2 > 0.9$, similar periods in both filters), the LC shape, and stellar luminosity. For each type of variable, we found around 1000 candidates. These objects were added to the remaining candidates to enhance their density in parameter space. We then selected Cepheids, RRab and RRc Lyrae, and δ Scuti stars based on their density of data points. In doing so, candidates located close to the best-established sample objects were assumed to be of the same type. This process was repeated until the density of the remaining candidates was similar to the density of variables with non-characteristic LCs in their vicinity. After removing these four types of variables, the majority of the remaining candidates were eclipsing binaries. We selected all eclipsing binaries with amplitudes larger than 0.08 mag to distinguish them from RS Canum Venaticorum-type systems (RS CVn), which are eclipsing binaries exhibiting chromospheric activity.

The LCs of eclipsing binaries are highly symmetric, and their phase differences do not deviate significantly from 2π ($|\phi_{21} - 2\pi| < 0.1\pi$) for periods longer than 0.3 days (half periods for eclipsing binaries²). However, contact (EW-type) eclipsing binary systems with half-periods shorter than 0.3 days show a more scattered distribution of ϕ_{21} . We retained these half-periods until we had completed the separation of eclipsing binaries from other types of variables. Since the number density of EW-type eclipsing binaries is higher than that of the other types of periodic variables (around 0.1–0.4% of the overall stellar population, depending on environment Rucinski 2006; Chen et al. 2016b), more than half of our candidates are eclipsing binaries. After removal of the eclipsing binaries, the remaining candidates were variables characterized by non-characteristic LCs. From short to long periods, they are low-amplitude δ Scuti (LAD) stars, RS CVn, BY Draconis (BY Dra)-type variables, semi-regular variables (SRs), and Miras. LADs

² The period determination process produces half-periods for the majority of eclipsing binaries because the two eclipses over a full period are too similar to be separated. Only very few eclipsing binaries with significantly modulated LCs yield full periods.

have shorter periods and brighter luminosities than their counterpart EW-type eclipsing binaries or RS CVn.

The LCs of RS CVn show an additional sine signal out-of-eclipse, which is the result of chromospheric activity. They have very similar luminosities to eclipsing binaries. BY Dras are K–M dwarf rotational stars also exhibit chromospheric activity. Their rotational periods range from less than one to a few days. Since almost all K–M dwarfs show BY Dra LCs, they are second in terms of their numbers only to EW-type eclipsing binaries in magnitude-limited samples. The period ranges of BY Dra and RS CVn overlap significantly; they can only be separated with the help of their luminosities. BY Dra are fainter than RS CVn. Their absolute magnitudes are concentrated in the range $2.8 < M_{Wgr} < 4.6$ mag. We also found that the luminosities of BY Dra have no relation to their periods, which means that stellar mass does not affect the rate of rotation among these objects. SRs are red giants, red supergiants, or asymptotic giant branch (AGB) stars with periodic and variable LCs. SR periods range from 20 to thousands of days, which overlaps significantly with the Mira period range. Miras are oxygen- or carbon-rich AGB stars. The DBSCAN results show that SRs and Miras can be separated because of an apparent difference in amplitude (see also Jayasinghe et al. 2018). Here, we selected Miras by adopting $\text{Amp}_r > 2$ mag or $\text{Amp}_g > 2.4$.

The criteria adopted to assist with the DBSCAN process are listed in Table 1. The ϕ_{21} – $\log P$ diagrams of all variables are shown in Figures 1 and 2. We find that aliased periods around one day are almost excluded. In Figure 2, variables with non-characteristic LCs exhibit a random distribution of ϕ_{21} between π and 3π . A low density in $-0.7 < \log P < 1.3$ [days] and $1.95\pi < \phi_{21} < 2.05\pi$ is due to the difficulty to separate non-characteristic LCs from eclipsing binaries’ LCs.

Eclipsing binaries can be divided into EW, semi-detached (EB), and detached (EA) types according to the degree by which they fill their Roche lobes. An accurate classification requires a detailed orbital analysis, which represents a major effort. Fortunately, we can also use well-established empirical relations related to their LCs. We refitted the LCs of our sample of eclipsing binaries using their full periods. The newly determined Fourier parameters a_2 and a_4 (similar to a_1 and a_2 pertaining to their half-periods) and the difference between the primary and secondary minimum magnitudes $\Delta_{\min} = m_p - m_s$ were obtained to perform the classification. Compared with EW-type eclipsing binaries, EA-type objects have a larger amplitude a_4 . To separate EW from EA types, we used the (a_4, a_2) diagram, similarly to Chen et al. (2018b).

We also adopted $R_{41} = a_4/a_2 = 0.43$ (see Figure 4) as additional boundary to identify eclipsing binaries that were not well separated based on the equations of Chen et al. (2018b). The main difference between semi-detached and contact eclipsing binaries is the difference between both minima. Both components of contact eclipsing binary systems share a common envelope and, as a result, they have similar temperatures. However, semi-detached eclipsing binaries usually exhibit larger Δ_{\min} because of the different temperatures of the two components. $\Delta_{\min} = 0.2$ mag (corresponding to a 5% difference between the components’ temperatures for an inclination of $i = 90^\circ$) is usually adopted as the boundary between semi-detached and contact eclipsing binaries. This criterion offers a rough classification of the two subtypes, and it is reliable for higher orbital inclinations ($i > 70^\circ$) and good photometric quality. We did not try to classify and distinguish semi-detached eclipsing binaries from other types of eclipsing binaries. Instead, we recorded the two-band minimum differences Δ_{\min} in our catalog to facilitate any further classification based on future DRs.

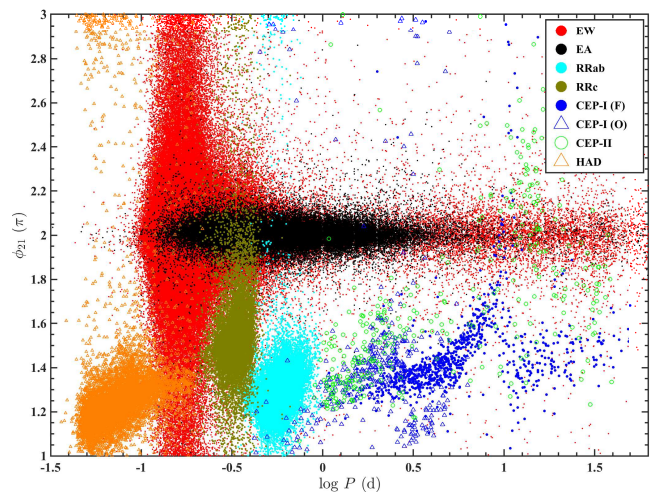


Figure 1. ϕ_{21} versus $\log P$ diagram for all ZTF variables with characteristic LCs. From short to long periods, these include high-amplitude δ Scuti stars (HADs: orange), EW-type eclipsing binaries (red), RRC Lyrae (dark green), RRab Lyrae (cyan), EA-type eclipsing binaries (black), first-overtone classical Cepheids (blue triangles), fundamental-mode classical Cepheids (blue dots), and Type II Cepheids (green circles).

The main subtypes of Cepheids among our candidates are classical Cepheids pulsating in their fundamental and first-overtone modes and Type II Cepheids. Classical and Type II Cepheids cannot be separated cleanly only based on LC information. However, classi-

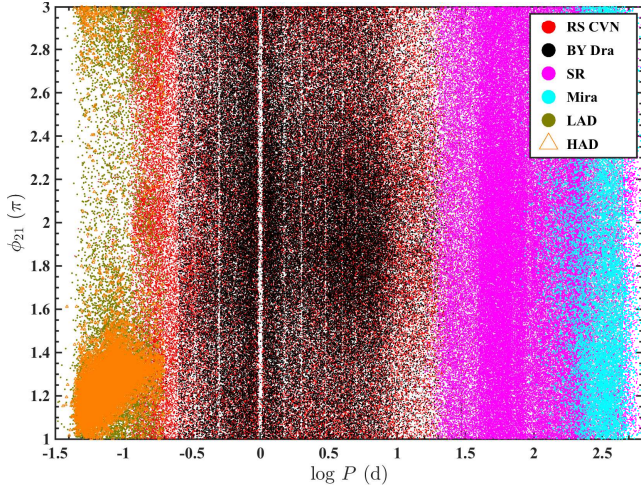


Figure 2. ϕ_{21} versus $\log P$ diagram for all ZTF variables with non-characteristic LCs. From short to long periods, these include low-amplitude δ Scuti stars (LADs: dark green), RS CVn (red), BY Dra stars (black), SRs (magenta), and Miras (cyan). Orange HADs are also shown, for comparison with the LADs.

cal Cepheids are two or three magnitudes brighter than Type II Cepheids. In addition, classical Cepheids are young and associated with the Milky Way’s thin disk. Armed with these two additional classification criteria, both Cepheid types can be separated more easily. The fundamental and first-overtone classical Cepheids exhibit different LC shapes. First-overtone Cepheids usually have smaller amplitudes ($\text{Amp.} < 0.4$ mag) and a low amplitude ratio ($R_{21} < 0.3$). In Figures 3 and 4, we can see a clear boundary between fundamental (blue dots) and first-overtone (blue triangles) classical Cepheids (see also Soszynski et al. 2008). Just like for Cepheids, RRab and RRC Lyrae pulsating in their fundamental and first-overtone modes also exhibit a clear boundary.

4.1. Luminosity Selection

Luminosity is the other important parameter one can use to classify variables. We present the period–luminosity diagram in Figure 5. Variables with *Gaia* parallax accuracy better than 20% are shown, except for the luminous variables, since most of the latter are distant and exceed our parallax constraint. Cepheids with $< 100\%$ parallax uncertainty, Miras with $< 50\%$ parallax uncertainty, and SRs with $< 50\%$ parallax uncertainty are shown. Variables outside these ranges exhibit more scatter in their absolute magnitude distributions and a tail at faint magnitudes, which is the result of the Lutz–Kelker effect.

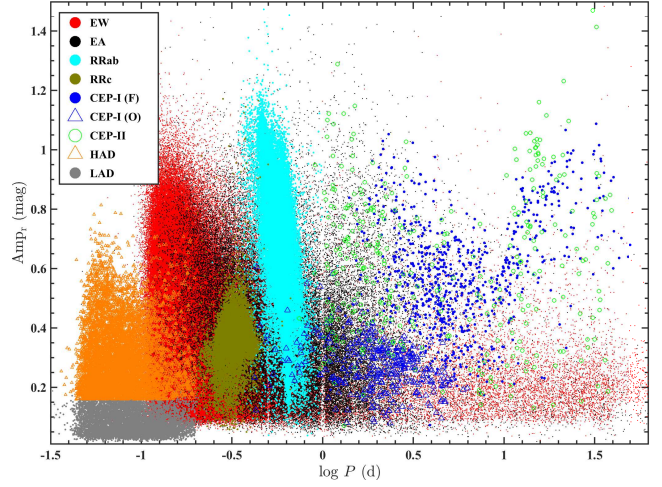


Figure 3. Amp_1 versus $\log P$ diagram for all ZTF variables. Symbols are as in Figure 1. LADs have been added as gray dots.

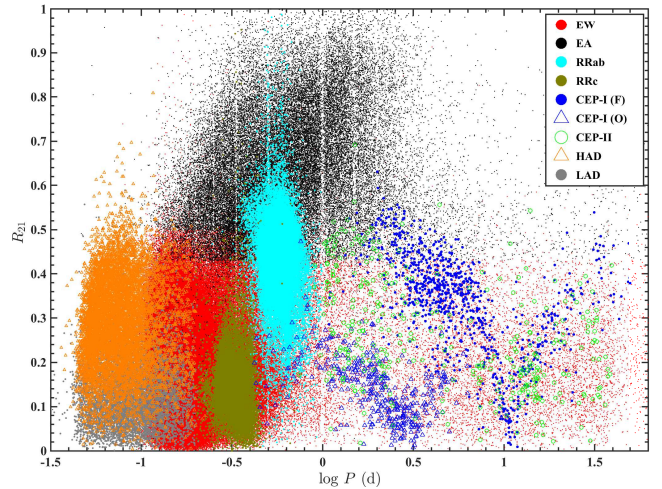


Figure 4. R_{21} versus $\log P$ diagram for all ZTF variables. Symbols are as in Figure 3.

δ Scuti stars, RRab and RRC Lyrae, and classical Cepheids that are located in the instability strip follow tight PLRs. The scatter in their absolute magnitudes is mainly caused by parallax uncertainties. We adopted $M_{W_{gr}} - M_{W_{gr}}(\text{PL}) < 3\sigma_{\text{DM}}$ to exclude dwarf contamination. Here, $M_{W_{gr}}$ and $M_{W_{gr}}(\text{PL})$ are the observed and predicted absolute magnitudes, respectively, and σ_{DM} is the error in the distance modulus, which has been propagated from the parallax uncertainty. The $M_{W_{gr}}(\text{PL}) - P$ relations for these variables were calculated using objects with parallax uncertainties less than 10%. Since these PLRs were roughly determined and only used to exclude contamination, we do not report the correspond-

ing coefficients here. For more accurate PLRs, we refer to individual papers discussed in Section 6.

In Figure 5, we find that both HADs and LADs follow similar PLRs, and their scatter seems smaller than that pertaining to the RR Lyrae and Cepheids. This smaller scatter is driven by the high number of nearby δ Scuti stars. Except for these variables, EW-type eclipsing binaries, Type II Cepheids, SRs, and Miras also follow PLRs characterized by moderate scatter. EW-type eclipsing binaries have been found to obey PLRs with 6–7% accuracy in infrared bands (Chen et al. 2016a, 2018a). SRs and Miras are LPVs that obey different sequences in the period–luminosity diagram (Lebzelter et al. 2019). Without access to accurate parallaxes and well-determined periods, their sequences are rather unclear.

At the bottom of the the period–luminosity diagram, we find that BY Dra variables are vertically distributed in the range of $2.8 < M_{W_{gr}} < 4.6$ mag, and they are fainter than other variables. This BY Dra sequence is always clear in a parallax-limited sample, which means that this is a real distribution rather than one caused by selection effects associated with the limit imposed on the *Gaia* parallaxes. Since the absolute magnitude boundary for BY Dra variables is unknown, we adopted these rough luminosity cuts to classify BY Dra stars. The rotational periods of BY Dra variables range from 0.25 to 20 days, with a peak around a few days. RS CVn occupy the same distribution as eclipsing binaries. They are not shown in the diagram. The PLRs or luminosity ranges were determined for each variable type to help with our classification. For example, candidates 2 mag fainter than classical Cepheids have a low probability of being classical Cepheids..

For candidates in the overlap region in parameter space, such as RRC and EW-type eclipsing binaries, Cepheids and rotational variables, LADs and EW-type eclipsing binaries, we performed a visual check of their LCs to assist with and confirm the classification process. We thus classified 781,602 periodic variables from our master sample of 2.1 million candidates. The remaining candidates were recorded as suspected variables. They will be better classified based on enhanced data from future ZTF DRs.

5. THE PERIODIC VARIABLES CATALOG

The periodic variables catalog³ of ZTF DR2, containing 781,602 periodic variables, is included in Table 2. It contains the source ID, position (J2000 R.A. and Dec.),

³ The full catalog and LCs can be accessed at <http://variables.cn:88/ztf/> or doi.org/10.5281/zenodo.3886372.

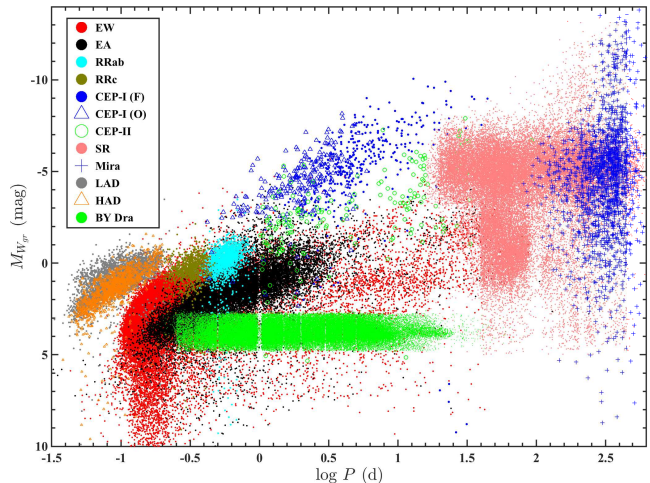


Figure 5. $\log P$ versus $M_{W_{gr}}$ diagram for variables with better than 20% (all variables except giants), 50% (Miras and SRs), and 100% (Cepheids) *Gaia* parallax accuracy. $M_{W_{gr}}$ are the absolute Weissenheit magnitudes estimated from a combination of g, r photometry and *Gaia* parallaxes. Symbols are as in Figure 4. Miras, SRs, and BY Dra variables have been added using blue plus signs, and pink and green dots, respectively.

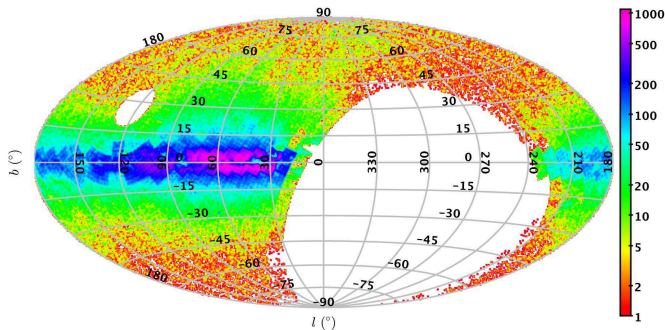
period, mean magnitudes ($\langle g \rangle$, $\langle r \rangle$), number of detections, LC parameters, and type of variable star. The LC parameters include the amplitude, amplitude ratio R_{21} , phase difference ϕ_{21} , Heliocentric Julian Date (HJD) of the minimum T_0 , R^2 of the LC fit, two-band minimum differences for eclipsing binaries, and the period’s FAP. Candidates without a good classification are collected in a suspected variables catalog (Table 6). The single-exposure photometry catalog is available online, including the objects’ SourceID, R.A. (J2000), Dec. (J2000), HJD, gmag, rmag, e_gmag, and e_rmag. Figure 6 shows the density distribution of these periodic variables in Galactic coordinates. This density distribution is similar to the distribution of the number of detections. 74% of the variables are located in the northern Galactic plane ($|b| < 10^\circ$), where variables have thus far not been recorded systematically.

5.1. New variables

We cross-matched our variables catalog with several other large variables catalogs to check the accuracy of our classification and of the derived periods, as well as the completeness of our catalog. The reference catalogs include the ASAS-SN Catalog of Variable Stars in the Northern Hemisphere, the ASAS-SN Catalog of Variable Stars with a reclassification of 412,000 known variables, the ATLAS catalog of variables, the *WISE* catalog of periodic variable stars, the Catalina catalog of

Table 1. Criteria adopted to classify different types of variables

Type	Selection criteria
LAD	$R^2 > 0.4$, Amp. < 0.2 , FAP < 0.001 , $M_{W_{gr}} - M_{W_{gr}}(\text{PL}) < 3\sigma_{\text{DM}}$, $P < 0.2$ days
HAD	$R^2 > 0.4$, Amp. > 0.2 , FAP < 0.001 , $M_{W_{gr}} - M_{W_{gr}}(\text{PL}) < 3\sigma_{\text{DM}}$
RRc	$R^2 > 0.6$, Amp. > 0.08 , FAP < 0.001 , $M_{W_{gr}} - M_{W_{gr}}(\text{PL}) < 3\sigma_{\text{DM}}$, $\phi_{21} < 1.9$
RRab	$R^2 > 0.6$, Amp. > 0.08 , FAP < 0.001 , $M_{W_{gr}} - M_{W_{gr}}(\text{PL}) < 3\sigma_{\text{DM}}$
Cepheid	$R^2 > 0.6$, Amp. > 0.08 , FAP < 0.001 , $M_{W_{gr}} - M_{W_{gr}}(\text{PL}) < 3\sigma_{\text{DM}}$, $P < 40$ days
Eclipsing binary	$R^2 > 0.4$, Amp. > 0.08 , FAP < 0.001
Mira	$R^2 > 0.4$, Amp. ≥ 2 , FAP < 0.001 , $P > 80$ days
SR	$R^2 > 0.4$, Amp. < 2 , FAP < 0.001 , $P > 20$ days
BY Dra	$R^2 > 0.4$, FAP < 0.001 , $2.8 < M_{W_{gr}} < 4.6$, $0.25 < P < 20$ days
RS CVn	$R^2 > 0.4$, FAP < 0.001 , $M_{W_{gr}} = M_{W_{gr}}(\text{Eclipsing binary})$, $P < 20$ days
EW	$a_4 \leq a_2(a_2 + 0.125)$ $a_2(a_2 + 0.125) < a_4 < a_2(a_2 + 0.375)$, $a_4/a_2 \leq 0.43$
EA	$a_4 \geq a_2(a_2 + 0.375)$ $a_2(a_2 + 0.125) < a_4 < a_2(a_2 + 0.375)$, $a_4/a_2 > 0.43$

**Figure 6.** Distribution map (in Galactic coordinates) of the 781,602 periodic variables classified in ZTF DR2.

periodic variable stars, the *Gaia* catalog of RR Lyrae and Cepheids, the OGLE variables catalog, and other variables collected in the General Catalogue of Variable Stars (GCVS). We assembled these catalogs and then used an angular radius of $2''$ to match the nearest known variables to our ZTF variables. Almost all objects were detected within $1''$, which means that the recent variable surveys all have good positional accuracy. In addition, a $1''$ matching radius can significantly reduce sample confusion, which is a potentially serious problem in dense fields. 621,702 of the 781,602 variables in the ZTF database are newly detected variables. The total number and the number of newly detected variables of each type are listed in Table 3. The new detection rate of these variables is high, ranging from 10% for RRab Lyrae to more than 90% for δ Scuti and BY Dra variables. This high new detection rate is not only the result of the database’s high photometric accuracy (~ 0.02 mag accuracy down to $r = 18$ mag) and the faint limiting magnitude of the ZTF database (about 1.5 mag deeper

than ATLAS in the corresponding r band) but also of the improvements made in our method of variable-star identification and classification. The relatively low new detection rate of RRab Lyrae is explained easily, because they were already well-covered by the Catalina survey and *Gaia* DR2. However, both the purity and the period accuracy of the RRab Lyrae are significantly improved in our ZTF catalog.

5.2. Classification Accuracy

The classification accuracy pertaining to each type of variable was tested by comparison with the four variable-star catalogs: see Table 4. The coincidence rates range from 95% to 99%, with any disagreement usually found at the faint end for each catalog. In addition, different sampling strategies may also result in somewhat inconsistent classifications. We note that a few (sub)types have relatively low coincidence rates of around 80%. This means that the standard of classification for these variables is not well-established. Among the four catalogs we compared our results with, the ASAS-SN catalog has the best classification accuracy overall.

In our catalog, RRab Lyrae have the best classification standard. Their purity is around 99%. The main contaminants are unsolved RRc Lyrae and EW-type eclipsing binaries. RRc Lyrae exhibit a purity of 91%. Their more symmetric LCs can easily mask them as EW-type eclipsing binaries. The purity of the eclipsing binaries is not as high as that of the RRab Lyrae. This is because of the difficulty in unequivocal classifications among the three binary subtypes. For lower LC amplitudes the classification becomes rather difficult. In this paper, we classify all eclipsing binaries into EW and EA types.

Table 2. ZTF Variables Catalog^a.

ID	R.A. (J2000)	Dec. (J2000)	Period days	R_{21}	ϕ_{21}	T_0	$\langle g \rangle$	$\langle r \rangle$...	Amp _g	Amp _r	Type
	°	°				HJD-2400000.5	mag	mag	...	mag	mag	
ZTFJ000000.13+620605.8	0.00056	62.10163	1.9449979	0.198	5.189	58386.2629478	17.995	16.571	...	0.113	0.078	BYDra
ZTFJ000000.14+721413.7	0.00061	72.23716	0.2991500	0.263	6.308	58388.2555794	19.613	18.804	...	0.540	0.438	EW
ZTFJ000000.19+320847.2	0.00080	32.14645	0.2870590	0.010	8.024	58280.4780813	15.311	14.610	...	0.219	0.197	EW
ZTFJ000000.26+311206.3	0.00109	31.20176	0.3622166	0.132	6.281	58283.4619944	16.350	15.844	...	0.233	0.226	EW
ZTFJ000000.30+233400.5	0.00125	23.56682	0.2698738	0.193	6.302	58437.2686640	17.890	16.944	...	0.373	0.352	EW
ZTFJ000000.30+711634.1	0.00125	71.27616	0.2685154	0.160	5.236	58657.4235171	19.144	17.875	...	0.173	0.154	EW
ZTFJ000000.39+605148.8	0.00163	60.86358	0.5591434	0.424	6.322	58338.4702019	19.965	19.002	...	0.797	0.841	EW
ZTFJ000000.51+583238.7	0.00215	58.54409	2.9797713	0.143	9.013	58663.4378649	16.586	15.368	...	0.082	0.068	BYDra
ZTFJ000001.00+612832.8	0.00420	61.47580	0.3643510	0.285	6.400	58385.2702714	20.640	19.627	...	0.970	0.681	EW
ZTFJ000001.37+561504.9	0.00571	56.25137	0.2557214	0.312	6.256	58471.1392038	19.416	18.559	...	0.674	0.623	EW
ZTFJ000001.74+614940.9	0.00729	61.82803	1.0158276	0.370	6.366	58349.3156217	19.094	18.013	...	0.289	0.228	EW
ZTFJ000001.75+594739.4	0.00732	59.79428	112.0533126	0.390	6.950	58320.7237689	18.676	17.393	...	0.062	0.055	SR
ZTFJ000001.92+554800.7	0.00804	55.80020	112.3366840	0.209	5.763	58389.1259060	12.664	0.0	...	0.114	0.0	SR
ZTFJ000002.02+540550.8	0.00844	54.09746	7.6299744	0.677	3.277	58472.1363770	18.176	17.187	...	0.187	0.151	RSCVN
ZTFJ000002.20+480720.8	0.00918	48.12246	0.3810135	0.227	3.701	58282.4549819	17.196	16.037	...	0.107	0.093	BYDra
ZTFJ000002.21+385226.4	0.00921	38.87401	0.4103992	0.168	6.512	58274.4798066	15.265	14.853	...	0.209	0.211	EW
ZTFJ000002.27+331411.5	0.00947	33.23655	0.1161226	0.069	3.714	58367.3685172	18.781	17.726	...	0.238	0.197	RSCVN
ZTFJ000002.28+592423.4	0.00954	59.40651	0.3286918	0.063	5.511	58314.4511431	20.860	19.268	...	0.280	0.255	EW
ZTFJ000002.61+560944.8	0.01091	56.16245	0.2780012	0.095	5.197	58644.4715685	16.017	15.664	...	0.074	0.074	RSCVN
ZTFJ000002.69+640614.8	0.01123	64.10413	0.4084968	0.250	6.617	58307.4094573	21.241	19.953	...	0.471	0.440	EW
ZTFJ000002.99+611736.0	0.01246	61.29334	0.5534820	0.269	6.289	58431.2049383	17.362	16.649	...	0.241	0.228	EW
ZTFJ000003.05+410045.6	0.01271	41.01267	0.2701826	0.236	6.311	58296.3618793	16.796	16.055	...	0.365	0.354	EW
ZTFJ000003.10+722838.4	0.01292	72.47736	0.2000857	0.014	5.677	58364.3618372	17.146	16.473	...	0.069	0.054	RSCVN
ZTFJ000003.13-022548.2	0.01306	-2.43006	0.4936916	0.431	3.906	58456.1669642	17.510	17.347	...	1.301	0.902	RR
ZTFJ000003.17+582138.3	0.01325	58.36065	331.9141625	0.334	6.273	58400.7947631	13.180	0.0	...	0.073	0.0	SR
ZTFJ000003.23+543605.4	0.01347	54.60151	0.7863971	0.105	8.826	58389.2748730	17.639	16.527	...	0.166	0.112	BYDra
ZTFJ000003.24+692214.2	0.01353	69.37062	0.3728018	0.169	6.048	58282.4524423	15.855	14.678	...	0.398	0.359	EW
ZTFJ000003.33+550558.3	0.01390	55.09955	0.2513022	0.377	6.044	58646.4653817	20.761	19.701	...	0.765	0.773	EW
ZTFJ000003.40+623837.5	0.01419	62.64377	0.2627338	0.288	6.245	58362.3199849	21.027	19.922	...	0.573	0.605	EW
ZTFJ000003.74+393925.9	0.01559	39.65722	0.2394832	0.050	7.755	58325.4868272	17.943	16.731	...	0.192	0.158	EW
ZTFJ000003.74+623637.4	0.01560	62.61040	0.3755206	0.344	6.383	58343.3639966	20.429	19.378	...	0.653	0.652	EW
ZTFJ000003.76+532917.1	0.01568	53.48811	0.5921959	0.408	7.638	58352.3259739	16.446	15.747	...	0.164	0.159	BYDra
ZTFJ000003.88+553759.9	0.01619	55.63331	0.2652778	0.341	6.266	58348.4098300	19.632	18.711	...	0.747	0.661	EW
ZTFJ000003.88+673554.8	0.01620	67.59858	7.8057274	0.096	6.155	58386.3788529	20.419	18.262	...	0.498	0.426	EW
ZTFJ000003.92+614456.1	0.01636	61.74894	0.3473332	0.272	6.092	58257.4187066	20.679	19.451	...	0.521	0.511	EW
ZTFJ000003.96+182425.2	0.01654	18.40700	0.4851359	0.456	3.909	58295.4504510	15.268	15.096	...	1.126	0.879	RR
ZTFJ000004.14+570616.8	0.01725	57.10468	246.2392553	0.319	3.591	58347.9920985	15.589	13.508	...	1.600	1.459	SR
ZTFJ000004.34+554359.8	0.01809	55.73328	0.3470882	0.272	6.349	58274.4650397	19.871	19.026	...	0.602	0.610	EW
ZTFJ000004.34+522031.5	0.01809	52.34209	4.0833915	0.189	7.602	58320.3673808	17.703	16.745	...	0.087	0.095	BYDra
ZTFJ000004.34+510505.0	0.01810	51.08474	0.3332412	0.034	4.458	58635.4032937	17.188	16.681	...	0.192	0.191	EW
ZTFJ000004.41+581846.9	0.01840	58.31303	0.4418413	0.126	3.603	58278.4683106	18.842	17.921	...	0.110	0.088	BYDra
ZTFJ000004.49+514615.4	0.01871	51.77095	0.0918632	0.187	4.174	58428.2433174	17.392	17.104	...	0.161	0.115	DSCT
ZTFJ000004.56+453022.7	0.01902	45.50633	6.6168334	0.084	6.243	58490.2445564	16.378	15.673	...	0.047	0.052	RSCVN
ZTFJ000004.98+524230.9	0.02076	52.70860	7.1420745	0.359	6.024	58471.1790394	17.357	15.933	...	0.080	0.072	BYDra
ZTFJ000005.00+555613.9	0.02087	55.93720	0.8834472	0.278	6.004	58332.3958118	18.238	16.738	...	0.141	0.131	EW
ZTFJ000005.13+503833.5	0.02138	50.64264	6.8118535	0.046	4.986	58316.3336707	16.984	16.128	...	0.125	0.072	BYDra
ZTFJ000005.21+650537.8	0.02174	65.09385	0.1251307	0.066	8.199	58353.4356974	14.071	13.139	...	0.107	0.070	DSCT
ZTFJ000005.34+543148.7	0.02228	54.53020	0.0602120	0.101	4.100	58305.4711181	14.514	14.305	...	0.080	0.055	DSCT
ZTFJ000005.74+573228.7	0.02393	57.54131	3.5412731	0.215	5.945	58304.4028037	16.206	15.416	...	0.060	0.059	BYDra
ZTFJ000005.94+555900.1	0.02479	55.98338	0.4009322	0.071	6.156	58354.4293181	17.257	16.647	...	0.167	0.175	EW
...
...
...
...

^aThe entire table is available in the online journal; 50 lines are shown here for guidance regarding its form and content.

Contamination by non-binaries is only 1%. This means that our separation of binaries from pulsators is efficient. EW-type eclipsing binaries have a purity of 96%; their main contaminants are EA-type eclipsing binaries. EA-type eclipsing binaries have a coincidence rate of 84%.

The coincidence rate of classical Cepheids is around 92%, based on a comparison of ~200 known Cepheids. The percentage of disagreement for Type II Cepheids is around 10%. LPV purity is around 98%. Here, the main misclassification occurs between SRs and Miras, even though all reference catalogs adopted a similar bound-

ary, Amp. = 2.0 mag. These different classifications can be explained by the different limiting magnitudes pertaining to the reference catalogs: a shallow limiting magnitude will lead to underestimated Mira amplitudes. For example, the ASAS-SN catalog has a limiting magnitude of 17, so that for Miras fainter than 15 mag, the amplitude determined is likely less than 2 mag. These Miras will hence be classified as SRs and, as a result, about 46% of matched Miras are mistaken for SRs in the ASAS-SN catalog. In turn, 99.2% of ASAS-SN Miras are correctly classified in our catalog. Toward the faint

magnitude limit of ZTF, this type of misclassification also occurs. In our catalog, 1694 SRs with $m_{g,r} > 19$ mag and $\text{Amp}_r > 1.0$ ($\text{Amp}_g > 1.2$) mag run the risk of misclassification.

The short-period δ Scuti variables have a purity of 88%. However, δ Scuti stars are not well classified in previously published catalogs. In our catalog, the purity of HADS is as high as those of RR Lyrae and eclipsing binaries, while the LADS purity is relatively lower. As regards rotational stars, the purity of BY Dra (93.7%) is high since they were strictly selected based on their *Gaia* parallaxes. However, without a luminosity criterion, it is not easy to separate RS CVn and eclipsing binaries with poor-quality photometry. To obtain a cleaner sample of eclipsing binaries, many eclipsing binaries with relatively poor-quality LCs have been classified as RS CVn, which leads to a systematically lower purity level of RS CVn (75.2%). Given that we have double checked the LCs of all variables where we noticed disagreement with other catalogs, our classification is more reliable for most of these objects. This is reasonable, since ZTF is deeper, has better-quality photometry, and has been obtained in two passbands. However, toward the faint end of the ZTF, the ZTF sample purity will also decrease.

Table 3. All and newly detected ZTF variables.

Type	Total	New (fraction)
Cep-I	1262	565 (44.8%)
Cep-II	358	154 (43.0%)
RRab	32,518	3034 (9.3%)
RRc	13,875	2178 (15.7%)
δ Scuti	16,709	15,396 (92.1%)
EW	36,9707	306,375 (82.9%)
EA	49,943	40,201 (80.5%)
Mira	11,879	4,997 (42.1%)
SR	119,261	97,737 (82.0%)
RS CVn	81,393	70,957 (87.2%)
BY Dra	84,697	80,108 (94.6%)
Total number	781,602	621,702 (79.5%)

5.3. Period Accuracy

ZTF DR 2 covers a timespan of 470 days, so the periods in our catalog are most accurate for $P \lesssim 100$ days. This limitation causes problems for the periods of SRs and Miras. Period problems pertaining to short-period variables are usually caused by the limited sampling cadence, e.g., a daily cadence is a major problem for ground-based time-domain surveys. Except for the

WISE catalog, the other three previously published catalogs and the ZTF catalog are all affected by this problem. This period problem is not easily eliminated by increasing the sampling using the same cadence, but it can be reduced based on multi-passband information and information about the physical properties of the variables. Figure 7 shows a comparison of the periods determined from the g and r LCs. One of the two periods is the real period (P_r), while the other is the aliased period (P_a). Both periods are found to mainly follow three relations: $1/P_a = |1/P_c \pm 1/P_r|$, $P_c = 0.5, 1, 2$ (corresponding to the red dotted, dashed, and solid lines in Figure 7, respectively). We can justify which period is more reliable, e.g., the bright variables are usually LPVs ($M_{Wgr} < -2$ mag), or variables with $\phi_{21} < 4$ are likely associated with R Rab rather than RRc periods. However, for eclipsing binaries and δ Scuti stars, there is no significant feature to validate the real period. For example, assuming that δ Scuti stars have real and aliased periods of 0.08 and 0.074 days, respectively, it is hard to justify which period is real, even with access to their luminosities and ϕ_{21} phases. Therefore, we visually compared the folded LCs pertaining to the two periods individually for those variables. This process can determine the correct period for most variables if the LC quality is good.

Our comparison of the four catalogs shows that our period accuracy is as high as 99%, except for LPVs and δ Scuti stars. The inconsistency rates for R Rab, RRc, EW-type eclipsing binaries, and for classical Cepheids, range from 0% to 2% (Table 5). This is a common accuracy for large variable-star catalogs. The inconsistency rate of δ Scuti stars is a little higher, since their periods are much shorter than the sampling cadence. Complementary short-cadence observations can resolve this aliased period problem. The full- versus half-period problem occurred for a few EA-type eclipsing binaries with insignificant secondary eclipses. If we do not consider the full- versus half-period problem, the period accuracy of EA-type eclipsing binaries is as high as those for other short-period variables. We have visually checked the LCs of EA-type eclipsing binaries to ensure that they all show the full periods. As to LPVs, around 11% of Miras and 32% of SRs have period differences larger than 20% by comparison with the ASAS-SN and Catalina catalogs. The precision of Mira periods is limited by the observational timespan. SRs usually contains several short- and long-term periods, so the low inconsistency derived here is not surprising. The accuracy of the LPV periods will be refined with the availability of future DRs.

Table 4. Variable purity comparison between ZTF and other catalogs.

Type	ATLAS	ASAS-SN	Catalina	WISE	Total sample
RRab	99.8%	98.6%	98.8%	96.2%	99.0%
RRc	89.0%	90.4%	93.9%		91.2%
EW	95.1% (99.8%) ^b	95.1% (97.1%)	97.1% (97.7%)	96.3% (98.4%)	95.6% (98.7%)
EA	82.0% (99.8%)	93.6% (96.0%)	70.5% (98.3%)	95.6% (98.5%)	84.3% (99.2%)
Cep-I	98.5%	84.1%		96.1%	91.7%
Cep-II	96.9%	82.8%	94.5%	88.1%	90.1%
SR	97.7%	98.0%			97.9%
Mira	88.5%	53.3%			69.3%
δ Scuti	83.5%	94.6%	85.5%		87.6%
RS CVn		75.2%			75.2%
BY Dra		93.7%			93.7%

^bThe purities in brackets only account for contamination by non-binary variables.

Table 5. Period comparison between ZTF and other catalogs.

Type	ATLAS	ASAS-SN	Catalina	WISE	Total sample
RRab	99.7%	99.7%	98.0%	99.6%	99.6%
RRc	98.9%	98.4%	97.8%		98.3%
EW	99.8%	98.6%	95.3%	99.9%	98.7%
EA	92.9% (98.7%) ^c	93.8% (99.4%)	95.1% (98.1%)	93.1% (99.7%)	93.2% (98.9%)
Cep-I	100%	97.9%		100%	99.2%
SR		68.3%	93.5%		68.4%
Mira		88.2%	94.6%		88.7%
δ Scuti	98.8%	94.8%	91.5%		96.6%

^cThe values in brackets do not take into account the full- versus half-period problem.

5.4. Completeness

We estimate the completeness of our catalog by comparison with previously published catalogs based on known variables in the ZTF magnitude range deemed reliable ($r > 12.5$ mag), as well as its spatial coverage (Dec. $> -13^\circ$). The completeness for the full sample is 71.1%. Since sampling of the ZTF is not homogeneous across the entire northern sky, the completeness varies with spatial position (see Figure 6). For regions at high declinations (Dec. $> 40^\circ$), the completeness can be as high as 76%. Some 24% of our variables are not classified because of insufficient sampling. The ZTF DR2 contains ~ 150 detections for each object, a smaller number than the equivalent numbers of detections in the ASAS-SN and Catalina catalogs. As the declination decreases, the completeness gradually decreases to 50%. For different magnitude ranges, the completeness is always around 71.1%, which means that the completeness is not affected by the objects' apparent magnitudes or

photometric uncertainties. With future DRs, ZTF will be able to detect and classify more than 1 million periodic variables in the northern sky, assuming current completeness levels. *Gaia* may be able to help classify 3 million periodic variables across the full sky, considering their enhanced density in the Galactic bulge and the Magellanic Clouds in the southern sky.

Except for spatial sampling, time sampling issues may also cause incompleteness. Since our catalog only covers a timespan of 470 days, its completeness for LPVs is not as high as that for short-period variables. We compare the LPVs in the ASAS-SN catalog with our sample to estimate their completeness, since ASAS-SN covers both a longer timespan and a larger number of LPVs. Globally, 42% of LPVs across the entire sky were rediscovered in our catalog. This fraction is some 30% lower than that for our full sample of variables.

5.5. Cepheids and RR Lyrae

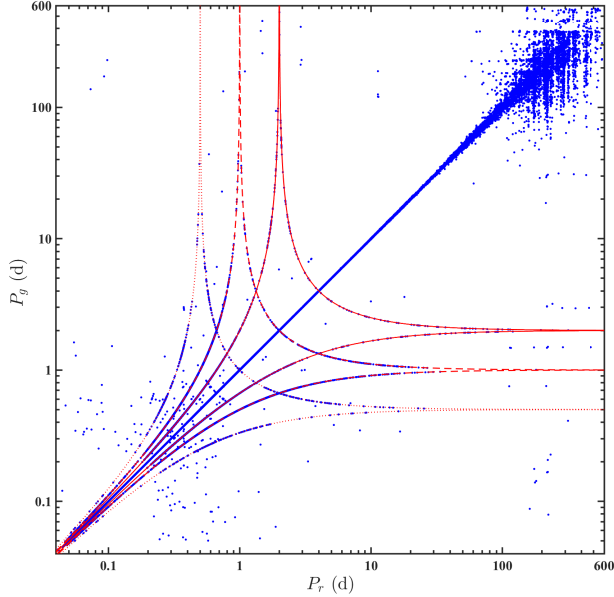


Figure 7. Comparison of periods determined from the g - and r -band LCs. The red lines are the predicted relations between real and aliased periods.

In addition to our comparisons with the four variables catalogs, we also evaluated the periods and completeness levels of the Cepheids and RR Lyrae in our catalog by comparison with the OGLE and *Gaia* catalogs, both of which have similar depths as ZTF. OGLE IV recently released their variables catalog of Cepheids and RR Lyrae in the Galactic disk (Skowron et al. 2019b; Soszyński et al. 2019). Although the overlap region between OGLE and ZTF is limited, a comparison is still feasible. *Gaia* DR2 contains about 140,000 RR Lyrae across the full sky, as well as 500 classical Cepheids in the Milky Way.

As for the classical Cepheids, we compared our catalog with the 2682 high-probability Cepheids collected by the OGLE team (Pietrukowicz et al. 2013; Udalski et al. 2018). The number of objects in common is 691, and the completeness of our ZTF Cepheids is 63.3% given that 1092 of the full sample of Cepheids are located in the ZTF’s detection region. This relatively low completeness level compared with the global completeness of our variables catalog suggests that the completeness of variable types with intermediate periods is lower than that of short-period variables. Only two of the 691 confirmed objects have inconsistent periods. Having double checked these periods, we conclude that our periods are more reliable.

OGLE IV contains 10,000 RR Lyrae in the Galactic disk, and two of their fields overlap with the field covered by the ZTF catalog. We found that 1327 of the 1854 (71.6%) OGLE RR Lyrae in these two fields

have been rediscovered in our catalog; 99.5% of these 1327 RR Lyrae have consistent periods. Both the period accuracy and completeness are in agreement with the equivalent values pertaining to the full catalog. For RR Lyrae contained in *Gaia* DR2, 39,301 are located in the ZTF’s detection region. Some 80.1% (31483) of *Gaia* RR Lyrae have been rediscovered in our catalog. This completeness level is 9% higher than the catalog’s global completeness of 71.1%, which is mainly driven by the incompleteness levels characteristic of *Gaia* RR Lyrae. About 400 of the *Gaia* RR Lyrae are contaminated by EW-type eclipsing binaries and δ Scuti stars.

6. DISCUSSION

In this section, we discuss for each type of variable their LCs, PLRs, and their applications as potential distance tracers.

6.1. Cepheids

Classical Cepheids are the most important primary distance tracers. They are widely used for estimating distances to galaxies in the Local Volume and measuring the near-field Hubble constant (Riess et al. 2019). Because of their young age, classical Cepheids are also the best stellar tracer of the Galactic disk. Compared with extragalactic Cepheids, Cepheids in our Milky Way are rare. Before 2018, only around 1000 Milky Way Cepheids had been detected (Pojmanski et al. 2005; Berdnikov 2008). These Cepheids were distributed within 3 kpc of the Sun and showed few features of our Milky Way’s structure. In 2018, several times the number of previously known classical Cepheids were found. The *WISE* catalog of variables listed about 1000 Cepheids that were homogeneously distributed across the Galactic plane, except for the Galactic Center direction. OGLE detected another one thousand Cepheids in the southern disk. ALTAS, ASAS-SN, and *Gaia* also detected several hundred Cepheids.

This rapid increase in the number of Cepheids motivated studies of the Milky Way’s disk. Samples of 1339–2500 carefully selected disk Cepheids revealed the first intuitive 3D map of our Galaxy’s stellar disk (Chen et al. 2019; Skowron et al. 2019a). The outer disk was found to be warped, and the warp is now known to be precessing (Chen et al. 2019). Recently, 640 new Cepheids in the southern disk affected by heavy extinction were discovered by the VVV survey (Dékány et al. 2019). In our ZTF catalog, we found an additional 565 new classical Cepheids, thus further enlarging the sample in the northern warp and around the edge of the disk. Figure 8 shows the distribution of 3300 well-determined disk classical Cepheids (satisfying the *Gaia* parallax

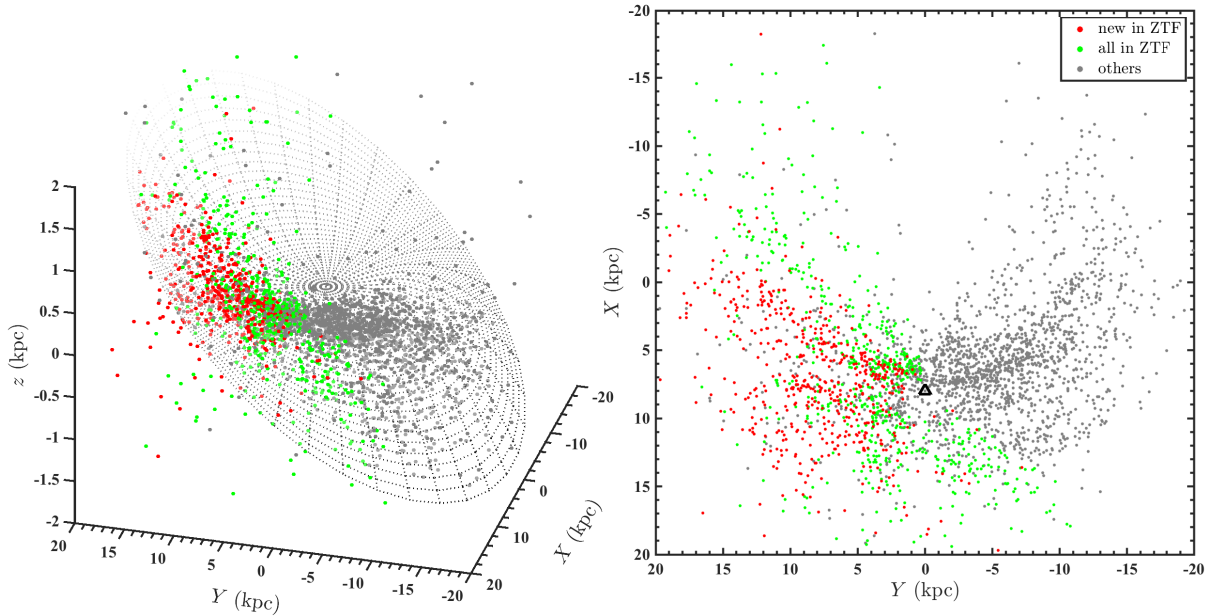


Figure 8. Milky Way disk in 3D (left) based on ~ 3300 Cepheids and their projection onto the (X, Y) plane (right). Red: new Cepheids in the ZTF catalog; green: other Cepheids in ZTF catalog; gray: Cepheids from OGLE, WISE, ATLAS, ASAS-SN, and other catalogs. The grid in the left-hand panel represents the warp model of Chen et al. (2019). The triangle in the right-hand panel denotes the position of our Sun.

and LC criteria), which agree with the warp model of Chen et al. (2019) to within $1-2\sigma$. This new sample of Cepheids is sufficient to trace the detailed morphology of the disk beyond Galactocentric distances of 15 kpc. In the (X, Y) plane, the Cepheid distribution is not homogeneous, but it shows bubble and filament features. A significant bubble is found at a distance of about 6 kpc from the Sun in the Galactic Anticenter direction. With a detailed study of these features, we could potentially infer the dynamical evolution history of the Galactic disk.

In the future, new Cepheids are expected to be found in the Galactic Center direction (Matsunaga et al. 2011; Dékány et al. 2015). In addition, low-amplitude or long-period Cepheids will be classified once more accurate parallaxes become available. Our larger sample of Cepheids will also be helpful in determining the zero points and slopes of their PLRs (Breuval et al. 2019), particularly of infrared PLRs (Chen et al. 2017; Wang et al. 2018). In addition to Cepheids in the Milky Way, we also found 21 Cepheids (one new Cepheid) associated with M31 (Kodric et al. 2018), one Cepheid in M33 (Hartman et al. 2006), and one in IC 1613 (Udalski et al. 2001). ZTF DR2 contains only about 50 detections in the M31 direction. With increased sampling in future DRs, several hundred Cepheids will likely be found in M31.

Cepheid LCs in g and r are shown in Figure 9. From their LCs, the majority of classical Cepheids can be

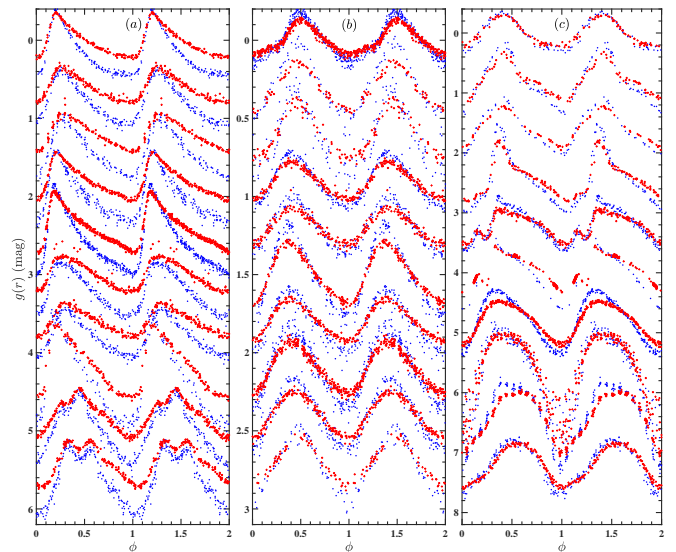


Figure 9. Example LCs for (a) fundamental-mode classical Cepheids, (b) first-overtone classical Cepheids, and (c) Type II Cepheids. The blue dots and red plus signs are LCs in the g and r bands, respectively. From top to bottom, phase differences ϕ_{21} increase. The mean magnitudes are fixed at $0.6i + 0.2$, $0.3i$, and $0.8i$ ($i = 0, 1, \dots, 9$) in the g band and $0.6i$, $0.3i$, and $0.8i$ in the r band, for fundamental-mode classical Cepheids, first-overtone classical Cepheids, and Type II Cepheids, respectively.

divided into fundamental-mode (Figure 9a) and first-overtone Cepheids (Figure 9b). First-overtone Cepheids

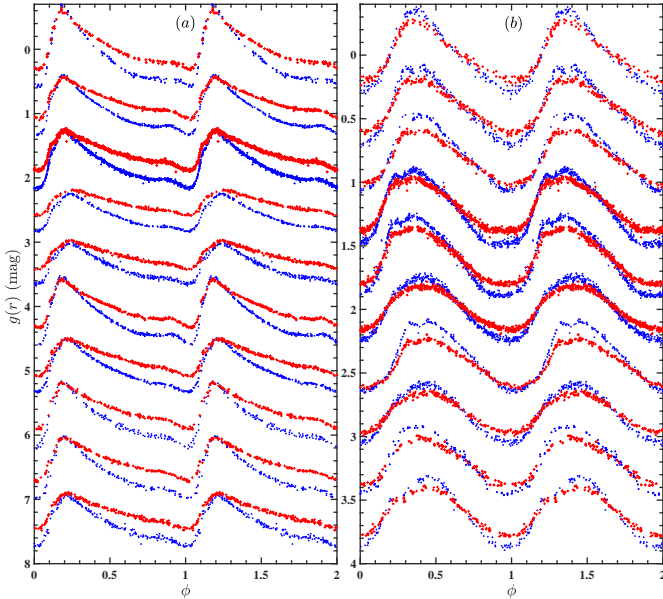


Figure 10. Example LCs for (a) RRab and (b) RRc Lyrae. The blue dots and red plus signs are LCs in the g and r bands, respectively. From top to bottom, phase differences ϕ_{21} decrease.

have lower amplitudes and shorter periods than the corresponding fundamental-mode Cepheids. At a given period, first-overtone Cepheids have slightly brighter luminosities. This magnitude difference is around 0.5 mag in the LMC (Inno et al. 2016), Small Magellanic Cloud (SMC Ripepi et al. 2017), and M31 (Kodric et al. 2018), while the situation in the Milky Way is less clear (Ripepi et al. 2019). With an increasing number of first-overtone Cepheids and better parallaxes, the PLRs of Milky Way Cepheids will be better constrained.

Compared with classical Cepheids, the LC shapes of Type II Cepheids are more highly variable (Figure 9c). Type II Cepheids are older, fainter, and follow PLRs characterized by a somewhat larger scatter (Groenewegen & Jurkovic 2017; Bhardwaj et al. 2017). Type II Cepheids are mostly located away from the disk and associated with the Galactic bulge and halo. As distance indicators, Type II Cepheids can be used to study the structure of the bulge (Braga et al. 2018a) and measure the distances to globular clusters and dwarf galaxies. We found 154 new Type II Cepheids, which represents a significant increase and will be useful to anchor their PLRs and explore old Galactic structures.

6.2. RR Lyrae

RR Lyrae are the most numerous distance indicators in old environments. Their PLRs or PL-metallicity relations can be as accurate as those for

the classical Cepheids (Catelan 2009, and references therein). In the Milky Way halo, RR Lyrae are used to trace dwarf galaxies and distant substructures (Drake et al. 2013; Sesar et al. 2017; Medina et al. 2018; Martínez-Vázquez et al. 2019; Erkal et al. 2019). RR Lyrae can be used to reveal structures out to distances of some 120 kpc. Better identification of RR Lyrae in the Dark Energy Survey can help to reach distances greater than 200 kpc (Stringer et al. 2019). RR Lyrae at moderate distances are usually used to determine accurate distances to globular clusters (Braga et al. 2018b; Bono et al. 2019; Palma et al. 2019). With a more complete sample, RR Lyrae are perhaps the best tracers to trace the Milky Way halo’s shape (Iorio et al. 2018; Iorio & Belokurov 2019). In the Galactic inner regions, featuring numerous RR Lyrae, the shape of the bulge can also be constrained (Pietrukowicz et al. 2015; Gran et al. 2016). In the ZTF catalog, we detected more than 5,000 new RR Lyrae out to distances of 125 kpc. We detected several RR Lyrae associated with the Draco dwarf galaxy at a distance of around 76 kpc (Bonanos et al. 2004). Unlike previous RR Lyrae samples, the new sample may reveal unknown structures at low Galactic latitudes ($|b| < 20^\circ$).

Studies of the physical properties of RR Lyrae will also benefit from large and complete samples. In recent years, many metal-rich RR Lyrae have been found (Chadid et al. 2017; Sneden et al. 2018), which challenge the traditional theory explaining these metal-poor and old variables. Both the WISE and ZTF catalogs focus on the Galactic disk; RR Lyrae in the disk are, with high probability, metal-rich. With LAMOST or SDSS-SEGUE spectra, the physical properties of a large sample of RR Lyrae can be investigated. In Figure 3, the distribution of RR Lyrae in the period–amplitude diagram is more scattered than dichotomous, which suggests that the well-known Oosterhoff dichotomy problem of RR Lyrae may just be due to a lack of intermediate-metallicity RR Lyrae (Fabrizio et al. 2019).

Similarly to classical Cepheids, most RR Lyrae can be divided into fundamental-mode (RRab) and first-overtone pulsators (RRc). Example LCs of RRab and RRc Lyrae are shown in Figure 10. The amplitudes of RRab Lyrae are larger, decreasing as the LCs become symmetric (from top to bottom in the left-hand panel of Figure 10). This trend is the result of the period–amplitude relation and is only significant for RRab LCs. The PLRs or PL–metallicity relations of Milky Way RRab Lyrae can be studied with *Gaia* DR2 parallaxes (Muraveva et al. 2018; Layden et al. 2019; Neeley et al. 2019). The accuracy of these PLRs is mainly limited by parallax uncertainties. RRc Lyrae also follow PLRs,

which are about 0.5 mag brighter than for RRab Lyrae at a given period. In Figure 5, RRc Lyrae seem to exhibit more scatter in their luminosities than RRab Lyrae. If we can better constrain the luminosities of RRc Lyrae, they may be potentially viable distance tracers. A number of RRab and RRc Lyrae exhibit multiple periods, and about one-third of the RRab Lyrae show period modulation. These special RR Lyrae will be analyzed with enhanced data from future DRs.

6.3. Eclipsing binaries

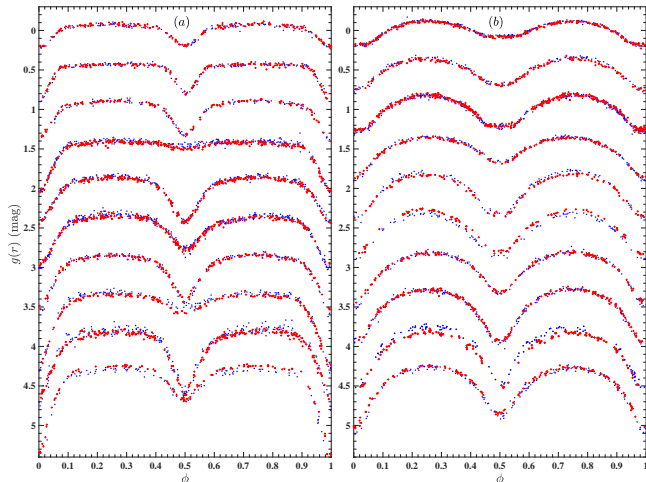


Figure 11. Example LCs for (a) EA- and (b) EW-type eclipsing binaries. The blue dots and red plus signs are LCs in the g and r bands, respectively. From top to bottom, the variation amplitudes increase.

The three types of eclipsing binaries are distinguished by their evolutionary stage. From EA- to EW-type eclipsing binaries, the period distribution gradually shifts to shorter periods. Statistically, EW-type eclipsing binaries tend to be older, with a peak in their age distribution around 4 Gyr. EA-type eclipsing binaries are young, with a peak age around 1 Gyr. The basic evolution of eclipsing binaries has recently become clear. Nuclear evolution and angular momentum loss are the main mechanisms (Hilditch et al. 1988; Nelson & Eggleton 2001; Yakut & Eggleton 2005; Stepien 2006; Jiang 2020). Both mechanisms run in parallel. Driven by angular momentum loss, the period decreases and both components become closer. When one component evolves to or away from the terminal main sequence, its radius increases. Until one component fills its Roche lobe, an EA-type eclipsing binary evolves to become an EB-type eclipsing binary. Then, with material and energy transferring from the primary to the secondary component, combined with possible mass re-

versal, the secondary component also fills its Roche lobe. The resulting system is an EW-type eclipsing binary. In Figure 1, the significant cut-off period of EW-type eclipsing binaries around 0.19 days is driven by the nuclear evolution timescale. The progenitor of the primary component of this 0.19-day EW-type eclipsing binary is a low-mass star with a nuclear evolution timescale very close to the age of the Galaxy.

Since their binary fraction is higher, eclipsing binaries account for a large proportion of variables in magnitude-limited samples. The fraction of EW-type eclipsing binaries was estimated at around 0.1% in the field (Rucinski 2006). It could be as high as 0.4% in a ~ 4 Gyr environment (Chen et al. 2016b). This fraction does not correct for the low-inclination problem and only counts EW-type eclipsing binaries seen at higher inclinations ($i > 40\text{--}60^\circ$). In our catalog, the fraction of EW-type eclipsing binaries identified is 0.07%, which is a lower limit. If we consider the number of missing EW-type eclipsing binaries owing to insufficient sampling (see Section 5.4), that fraction can be as high as 0.1%.

Detached eclipsing binaries evolve on timescales as long as or even longer than those of EW-type eclipsing binaries. However, depending on the spatial separation and radius ratio of both components, we can only observe eclipses of detached eclipsing binaries with $i \sim 90^\circ$. Consequently, the fraction of EA-type eclipsing binaries is lower than that of EW types. EB-type eclipsing binaries have the shortest evolution timescale and account for the lowest fraction among the three types of eclipsing binaries.

Figure 11 shows LCs of eclipsing binaries. Their shapes and amplitudes in both bands are almost the same and differ from those of pulsating stars. In the left-hand panel, we can identify when the eclipses start in the LCs of EA-type eclipsing binaries. In the right-hand panel, the eclipse onset in EW(EB)-type eclipsing binary LCs is hard to identify. In the period range of 0.25–0.56 days, EW-type eclipsing binaries follow tight infrared PLRs (Chen et al. 2018a) and can be potential distance indicators. The viability of these PLRs has been validated by eclipsing binaries from the ASAS-SN catalog (Jayasinghe et al. 2019a).

In Figure 5, about 90,000 EW-type eclipsing binaries with $< 20\%$ *Gaia* parallax uncertainties are found to also follow a PLR. In theory, the PLR of EW-type eclipsing binaries is driven by both Roche lobe theory and the mass–luminosity relation. Based on this PLR and a sample of several 100,000 EW-type eclipsing binaries, a better study of the detailed structure of the Milky Way will be possible. Except for distance determina-

tion, EW-type eclipsing binaries can also provide age information based on their periods. In addition, kinematic properties derived from *Gaia* data can provide constraints on the binaries’ ages (Hwang & Zakamska 2019). We expect that the eight-dimensional parameter space pertaining to EW-type eclipsing binaries can be established and used to constrain the Milky Way’s evolution. Without strict constraints on the secondary components, the PLR of EB-type eclipsing binaries exhibits more significant scatter. Less evolved, EA-type eclipsing binaries are the best objects to obtain absolute parameters from the orbital equations. By analyzing both their LCs and radial velocity curves, late-type EA-type eclipsing binaries can yield distances with 1% accuracy (Pietrzyński et al. 2019).

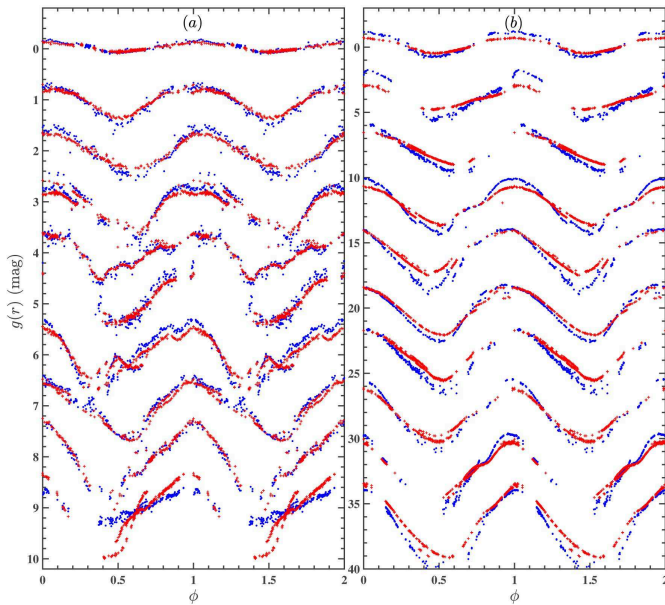


Figure 12. Example LCs for (a) SRs and (b) Miras. The blue dots and red plus signs are LCs in the g and r bands, respectively. From top to bottom, the variation amplitudes increase. The mean magnitudes are fixed at $1.0i$ and $4.0i$ ($i = 0, 1, \dots, 9$) in the g and r bands, for SRs and Miras, respectively.

6.4. SRs and Miras

SRs and Miras are most likely red giants, red supergiants, or AGB stars exhibiting long-period luminosity variations. They are important distance tracers in the context of the cosmological distance scale since they are brighter than classical Cepheids in infrared bands. However, LPVs follow multi-sequence PLRs, and each PLR sequence exhibits larger scatter (Lebzelter et al. 2019) than the classical Cepheid PLRs. To become a reli-

able distance indicator, LPV properties must be studied in more detail, particularly in the Milky Way and M31. The PLRs of red supergiants belonging to the LMC, SMC, M31, and M33 have been well-studied, and their 1σ accuracy is 10–15% in infrared bands (Yang & Jiang 2011, 2012; Ren et al. 2019). However, in the Milky Way, the number of red supergiants with reliable distances is too small to establish reliable PLRs (Chatys et al. 2019).

Oxygen-rich Miras also follow tight PLRs. In infrared bands, the 1σ scatter about their PLRs is around 10% (Yuan et al. 2017, 2018). Compared with red supergiants, Miras are 0–4 mag fainter but several times more numerous. All of these LPVs are potential tracers to measure the Hubble parameter (Huang et al. 2019). In the Milky Way, LPVs are young and intermediate-age structure tracers, complementary to Cepheids and RR Lyrae. Similarly to eclipsing binaries, the ages of each LPV subtype can be inferred from their periods (Mowlavi et al. 2018). As such, LPVs are also tracers that can constrain the evolution history of our Galaxy.

LCs of SRs and Miras are shown in the left- and right-hand panels of Figure 12, respectively. In the ZTF, several Miras are found with r -band amplitudes exceeding 6 mag. Since the total timespan of the ZTF DR2 is 470 days, many Miras only have LCs available for at most one period. We detected about 130,000 LPVs, with the majority belonging to our Galaxy or to nearby dwarf galaxies. To better understand the physics of these LPVs, we also show them in color–magnitude and color–color diagrams (Figure 13a,b). *WISE* W_1 , $W_1 - W_2$, and $W_2 - W_3$ magnitudes with good photometric signal-to-noise ratios ($\text{SNR}_{W_1} > 5$, $\text{SNR}_{W_2} > 5$, $\text{SNR}_{W_3} > 10$) and quality were adopted to indicate LPV magnitudes and colors. This choice reduces the effects of the significant extinction in the Galactic plane. By comparison with massive stars in the LMC in color–absolute magnitude space (Yang et al. 2018), we find that SRs (blue dots in Figure 13) are composed of red giants, red supergiants, oxygen- and carbon-rich AGB stars, as well as extremely carbon-rich AGB stars. Miras (red dots) contain a few oxygen-rich, a few extremely carbon-rich, and many carbon-rich AGB stars.

AGB populations are characterized by an absolute magnitude of about -8 mag in the mid-infrared, and the bright end of the red supergiant population is around -12 mag. Therefore, data points with magnitudes brighter than -12 mag in the left-hand panel ($W_1 - W_2 < 0$) or brighter than -9 mag in the right-hand panel ($W_1 - W_2 > 0$) are stars that may have larger parallax uncertainties. In Figure 13c, the amplitudes grow monotonously as the periods increase. In

particular, some sequences are found in the SR distribution, referred to as the A, B, and C' (third, second, and first overtone) sequences (Trabucchi et al. 2017). Miras and some SRs form sequence C, which is the location of high-amplitude fundamental pulsators. In Figure 13d, SRs and Miras are separated by a boundary, with Miras being high-amplitude and red. The detailed subtype classification of these LPVs is not further discussed in this paper as it requires access to better periods and parallaxes.

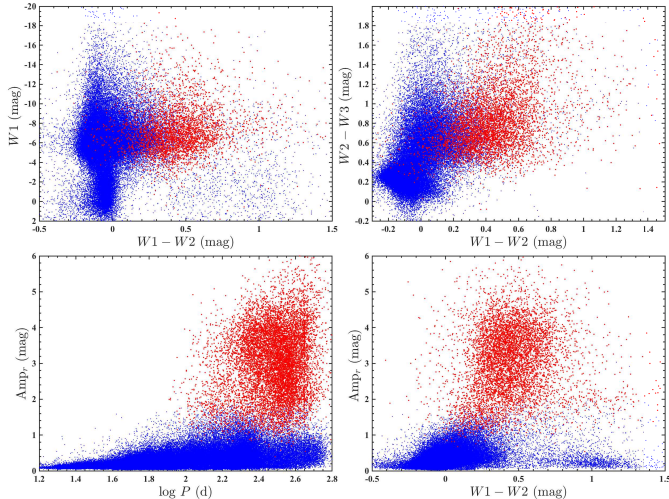


Figure 13. LPVs in the ZTF catalog. (a) Color–absolute magnitude diagram. (b) Color–color diagram. (c) Period–amplitude diagram. (d) Color–amplitude diagram. SRs and Miras are shown as red and blue dots, respectively.

6.5. δ Scuti stars

Among the variables in the ZTF, δ Scuti stars have the shortest periods. δ Scuti stars are main-sequence pulsators located in the instability strip, so they follow a PLR similar to RR Lyrae and Cepheids. Different from RR Lyrae and Cepheids, a fraction of δ Scuti stars is thought to exhibit multiple periods. The PLRs of δ Scuti stars are not well studied, even for HADs, because of their fainter magnitudes and limited sampling in the past. In the LMC, the magnitude range of δ Scuti stars ranges from 20 to 22 mag in the R band (Garg et al. 2010), which is close to the limiting magnitude of many time-domain surveys. PLRs of δ Scuti stars are therefore best studied in the Milky Way. Ziaali et al. (2019) tried to establish a V -band PLR based on 1100 δ Scuti stars in the *Kepler* field with good *Gaia* DR2 parallaxes; however, their PLR is not as tight as the equivalent PLRs pertaining to other tracers. Recently, Jayasinghe et al. (2020b) derived multi-band PLRs for fundamental and

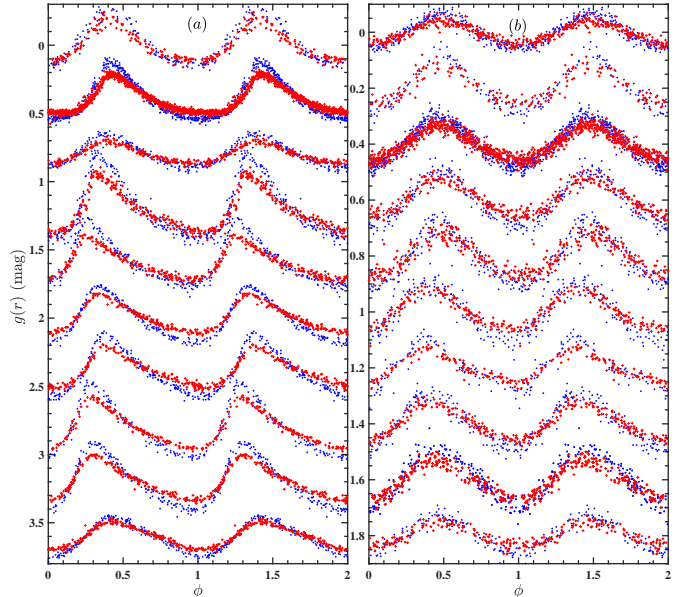


Figure 14. Example LCs for (a) HADs and (b) LADs. The blue dots and red plus signs are LCs in the g and r bands, respectively. From top to bottom, phase differences ϕ_{21} increase. The mean magnitudes are fixed at $0.4i$ and $0.2i$ ($i = 0, 2, \dots, 9$) in the g and r bands, for HADs and LADs, respectively.

overtone pulsators, based on ~ 8400 δ Scuti stars from ASAS-SN, and found a 1σ scatter around 10%.

Our ZTF sample is several times larger and more homogeneously distributed across the northern sky, which paves the way to improve the δ Scuti PLRs. In Figure 5, we show that the Wesenheit PLR of δ Scuti stars is tight, with few outliers. A simple estimation shows that the 1σ scatter of the HADs is around 10%. This means that the δ Scuti PLR is tighter in infrared bands. This is similar to the situation for other variables that follow PLRs. A forthcoming paper will investigate the multi-band PLRs of a large sample of δ Scuti stars. As distance indicators, δ Scuti stars cover a wide age range (according to their masses). Old δ Scuti (SX Phoenicis) stars can be used to measure the distances to globular clusters and nearby dwarf galaxies (McNamara 2011). Young or intermediate-age δ Scuti stars are found in open clusters (Wang et al. 2015), and they are potential tracers for studies of the Milky Way disk’s structure.

In Figure 14, HADs exhibit tooth-saw-shaped LCs similar to RR Lyrae and Cepheids (left-hand panel), while LADs show various types of LCs. Based on their LCs (Figures 3 and 4) alone, it is difficult to separate fundamental-mode and first-overtone δ Scuti stars. However, similarly to RR Lyrae and classical Cepheids, first-overtone δ Scuti stars are generally brighter than

fundamental-mode δ Scuti stars. The boundary between HADs and LADs is not clear. In the period–luminosity diagram (Figure 5), LADs also follow a PLR and are a little brighter than HADs. All these features imply that HADs and LADs are first-overtone and fundamental-mode δ Scuti stars, respectively, while their boundary is rather obscure. More properties of δ Scuti stars will be revealed by high-order frequency analysis with increased sampling in the next ZTF DR.

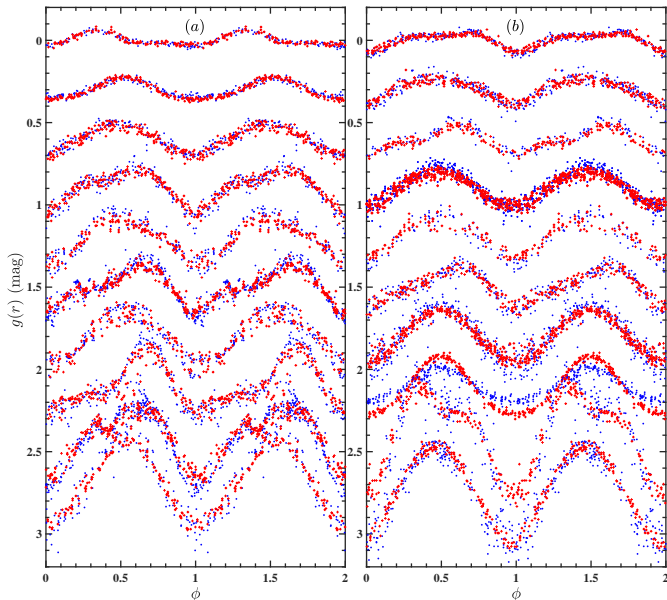


Figure 15. Example LCs for (a) RS CVn and (b) BY Dra stars. The blue dots and red plus signs are LCs in the g and r bands, respectively. From top to bottom, the variation amplitudes increase. The mean magnitudes are fixed at $0.3i$ ($i = 0, 1, \dots, 9$) in the g, r bands for both RS CVn and BY Dra stars.

6.6. RS CVn and BY Dra

Both RS CVn and BY Dra exhibit periodic but non-characteristic LCs (Figure 15). Their amplitudes or luminosities can be used to classify them. The LCs of RS CVn and BY Dra in the two different bands are similar. However, the overall shapes of their LCs are no longer symmetric about phase $\phi = 0.5$ or $\phi = 1.5$ (in most cases). A number of these variables have been detected in the ASAS-SN Catalog of the Southern Hemisphere (Jayasinghe et al. 2020a), where the authors treat them as rotational stars. Iwanek et al. (2019) also studied 12,660 spotted variable stars along the line of sight to and inside the Galactic bulge, based on OGLE data. Most of their variables are giant stars. In this paper, we divided these variables based on their different luminosities. RS CVn are F–G-type eclipsing binaries with

strong chromospheric activity. Their spectra show Ca II H and K emission (Hall 1976). The LCs of RS CVn are a combination of eclipses and spot modulation. RS CVn have thus far only been studied based on small sample sizes (Zhang et al. 2014). Therefore, our catalog of $\sim 80,000$ RS CVn is the best sample to investigate these objects’ properties statistically. A new discovery already resulting from this enlarged sample is that RS CVn have a wider period distribution than previously inferred (Hall & Kreiner 1980; Dempsey et al. 1993; Donati et al. 1997). In Figure 2, for all periods, eclipsing binaries have the highest probability of having RS CVn features. Nevertheless, the peak of the RS CVn log P distribution occurs around a few days, which is much longer than that for eclipsing binaries (0.3–0.4 days).

BY Dra stars are also variables featuring chromospheric activity, but they are of K–M type and fainter than RS CVn. Several papers have studied BY Dra and some RS CVn stars based on samples of a few hundred objects (Strassmeier et al. 1993; Eker et al. 2008; Hartman et al. 2011). However, criteria to separate the two types of variables are not well-established. In our sample, with the help of *Gaia* parallaxes, BY Dra stars are predominantly distributed in a narrow magnitude range, $2.8 < M_{W_{gr}} < 4.6$ mag (Figure 5). The period range of BY Dra stars is narrower than that of RS CVn variables. As for the overall distributions of periods and amplitudes, both types of variables exhibit similar features. A better study of RS CVn and BY Dra variables will be achieved with a combination of LCs and spectra.

7. CONCLUSIONS

ZTF DR2 contains about 0.7 billion objects with more than 20 exposures each. As such, ZTF DR2 represents a highly suitable database for the detection and exploration of new variable stars. In this paper, we have adopted the Lomb–Scargle periodogram approach to search for periodic variables. We obtained a sample of 1.4 million candidates with FAP < 0.001 . Following exclusion of candidates with aliased periods and poor-quality LCs, ~ 1.0 million candidates remained for classification. Classification was done using the DBSCAN method based on the distributions of the objects’ periods, LC parameters, and luminosities. We classified 781,602 periodic variables into δ Scuti, EW- and EA-type eclipsing binaries, RRab and RRC Lyrae, classical Cepheids, Type II Cepheids, SRs, and Miras. After cross-matching with known variables, 621,702 of the 781,602 objects turned out to be newly detected variables. This high new detection rate highlights both the

Table 6. ZTF Suspected Variables Catalog.

ID	R.A. (J2000) °	Decl. (J2000) °	$\langle g \rangle$ mag	$\langle r \rangle$ mag	Period _g days	Period _r days	Amp _g mag	Amp _r mag	Num _g	Num _r	log (FAP) _g
ZTFJ000000.06+583327.2	0.00026	58.55756	12.974	12.324	1.00157	0.05415	0.059	0.057	118	137	-5.865
ZTFJ000000.09+632559.3	0.00041	63.43315	15.137	14.451	339.5882	344.55948	0.075	0.038	124	146	-6.685
ZTFJ000000.14+552150.6	0.00060	55.36408	17.081	15.919	0.49772	0.09674	0.049	0.024	121	143	-5.067
ZTFJ000000.15+540322.4	0.00066	54.05624	18.144	16.776	0.49768	0.10488	0.087	0.023	122	144	-5.566
ZTFJ000000.16+621059.7	0.00069	62.18326	16.454	15.585	0.4979	0.08946	0.046	0.018	125	146	-5.494
ZTFJ000000.17+592103.3	0.00073	59.35093	17.342	16.391	0.99392	0.13364	0.055	0.026	124	147	-4.545
ZTFJ000000.25+605628.0	0.00108	60.94112	17.745	15.993	0.99385	0.44865	0.127	0.019	125	146	-3.811
ZTFJ000000.27+665503.0	0.00116	66.91750	16.711	15.505	251.12632	0.05878	0.069	0.021	169	186	-6.459
ZTFJ000000.28+583810.1	0.00119	58.63614	15.121	14.359	295.46337	0.33318	0.068	0.059	118	138	-5.534

NOTE—(This table is available in its entirety in machine-readable form.)

high quality of the ZTF photometry and the improvement of our classification method.

Checks of the periods and types contained in our catalog show that they are better than or as good as the same parameters contained in previously published catalogs. The sampling completeness is not homogeneous in the northern sky due to the observation mode adopted, ranging from 76% at high declinations to 50% in low declination regions (Dec. $< 0^\circ$). The completeness of LPVs is 30% lower than that of the full sample. For each variable type, our catalog represents a significant increase in sample size. The new variables will aid studies of the physics of variable stars as such, of the Milky Way's structure and evolution, and of the cosmological distance scale, particularly based on a combination of LCs and spectra.

Future ZTF DRs will cover both increased timespans and larger numbers of exposures. These aspects will help improve the determination of the LPV periods and increase the completeness of the catalog. LCs associated with double modes or amplitude (period) modulation will be re-analyzed when enhanced sampling becomes available. In addition to the main types of variables discussed here, there are many cataclysmic variables, low-amplitude pulsating stars, binaries with compact objects, and stars with exoplanets in the ZTF database. These variables will be identified to construct a large sample for further study based on future ZTF DRs.

ACKNOWLEDGMENTS

We thank the anonymous referee for comments that helped us improve the paper. This publication is based on observations obtained with the Samuel Oschin 48-inch Telescope at the Palomar Observatory as part of the Zwicky Transient Facility project. ZTF is supported by the National Science Foundation under grant AST-1440341 and a collaboration including Caltech, IPAC, the Weizmann Institute for Science, the Oskar Klein Center at Stockholm University, the University of Maryland, the University of Washington, Deutsches Elektronen-Synchrotron and Humboldt University, Los Alamos National Laboratories, the TANGO Consortium of Taiwan, the University of Wisconsin at Milwaukee, and Lawrence Berkeley National Laboratories. Operations are conducted by COO, IPAC, and UW. We are grateful for research support from the National Natural Science Foundation of China through grants 11903045, U1631102, and 11633005. This work was supported by the National Key Research and Development Program of China through grant 2017YFA0402702. We also thank Dr. Changqing Luo and Dr. Fan Yang for providing computing time.

REFERENCES

- Akerlof, C., Amrose, S., Balsano, R., et al. 2000, *AJ*, 119, 1901
- Allcock, C., Akerlof, C. W., Allsman, R. A., et al. 1993, *Nature*, 365, 621
- Bellm, E. C., Kulkarni, S. R., Barlow, T., et al. 2019, *PASP*, 131, 068003
- Berdnikov, L. N. 2008, *VizieR Online Data Catalog*, II/285
- Bhardwaj, A., Rejkuba, M., Minniti, D., et al. 2017, *A&A*, 605, A100
- Bonanos, A. Z., Stanek, K. Z., Szentgyorgyi, A. H., Sasselov, D. D., & Bakos, G. Á. 2004, *AJ*, 127, 861
- Bono, G., Iannicola, G., Braga, V. F., et al. 2019, *ApJ*, 870, 115
- Braga, V. F., Bhardwaj, A., Contreras Ramos, R., et al. 2018a, *A&A*, 619, A51
- Braga, V. F., Stetson, P. B., Bono, G., et al. 2018b, *AJ*, 155, 137

- Breuval, L., Kervella, P., Arenou, F., et al. 2019, arXiv e-prints, arXiv:1910.04694
- Burdge, K. B., Coughlin, M. W., Fuller, J., et al. 2019, *Nature*, 571, 528
- Catelan, M. 2009, *Ap&SS*, 320, 261
- Chadid, M., Sneden, C., & Preston, G. W. 2017, *ApJ*, 835, 187
- Chambers, K. C., Magnier, E. A., Metcalfe, N., et al. 2016, arXiv e-prints, arXiv:1612.05560
- Chatys, F. W., Bedding, T. R., Murphy, S. J., et al. 2019, *MNRAS*, 487, 4832
- Chen, X., de Grijs, R., & Deng, L. 2016a, *ApJ*, 832, 138
- . 2017, *MNRAS*, 464, 1119
- Chen, X., Deng, L., de Grijs, R., Wang, S., & Feng, Y. 2018a, *ApJ*, 859, 140
- Chen, X., Wang, S., Deng, L., et al. 2019, *Nature Astronomy*, 3, 320
- Chen, X., Wang, S., Deng, L., de Grijs, R., & Yang, M. 2018b, *ApJS*, 237, 28
- Chen, X., Deng, L., de Grijs, R., et al. 2016b, *AJ*, 152, 129
- Cioni, M. R. L., Clementini, G., Girardi, L., et al. 2011, *A&A*, 527, A116
- Clementini, G., Ripepi, V., Molinaro, R., et al. 2019, *A&A*, 622, A60
- Cui, X.-Q., Zhao, Y.-H., Chu, Y.-Q., et al. 2012, *Research in Astronomy and Astrophysics*, 12, 1197
- Dékány, I., Hajdu, G., Grebel, E. K., & Catelan, M. 2019, *ApJ*, 883, 58
- Dékány, I., Minniti, D., Majaess, D., et al. 2015, *ApJL*, 812, L29
- Dempsey, R. C., Linsky, J. L., Fleming, T. A., & Schmitt, J. H. M. M. 1993, *ApJS*, 86, 599
- Deng, L.-C., Newberg, H. J., Liu, C., et al. 2012, *Research in Astronomy and Astrophysics*, 12, 735
- Donati, J. F., Semel, M., Carter, B. D., Rees, D. E., & Collier Cameron, A. 1997, *MNRAS*, 291, 658
- Drake, A. J., Catelan, M., Djorgovski, S. G., et al. 2013, *ApJ*, 765, 154
- Drake, A. J., Graham, M. J., Djorgovski, S. G., et al. 2014, *ApJS*, 213, 9
- Drake, A. J., Djorgovski, S. G., Catelan, M., et al. 2017, *MNRAS*, 469, 3688
- Eisenstein, D. J., Weinberg, D. H., Agol, E., et al. 2011, *AJ*, 142, 72
- Eker, Z., Ak, N. F., Bilir, S., et al. 2008, *MNRAS*, 389, 1722
- Erkal, D., Belokurov, V., Laporte, C. F. P., et al. 2019, *MNRAS*, 487, 2685
- Fabrizio, M., Bono, G., Braga, V. F., et al. 2019, *ApJ*, 882, 169
- Gaia Collaboration, Brown, A. G. A., Vallenari, A., et al. 2018, *A&A*, 616, A1
- Gaia Collaboration, Eyer, L., Rimoldini, L., et al. 2019, *A&A*, 623, A110
- Garg, A., Cook, K. H., Nikolaev, S., et al. 2010, *AJ*, 140, 328
- Graham, M. J., Djorgovski, S. G., Stern, D., et al. 2015, *Nature*, 518, 74
- Graham, M. J., Kulkarni, S. R., Bellm, E. C., et al. 2019, *PASP*, 131, 078001
- Gran, F., Minniti, D., Saito, R. K., et al. 2016, *A&A*, 591, A145
- Groenewegen, M. A. T., & Jurkovic, M. I. 2017, *A&A*, 604, A29
- Hall, D. S. 1976, in *Astrophysics and Space Science Library*, Vol. 60, IAU Colloq. 29: Multiple Periodic Variable Stars, ed. W. S. Fitch, 287
- Hall, D. S., & Kreiner, J. M. 1980, *AcA*, 30, 387
- Hartman, J. D., Bakos, G. Á., Noyes, R. W., et al. 2011, *AJ*, 141, 166
- Hartman, J. D., Bersier, D., Stanek, K. Z., et al. 2006, *MNRAS*, 371, 1405
- Heinze, A. N., Tonry, J. L., Denneau, L., et al. 2018, *AJ*, 156, 241
- Hilditch, R. W., King, D. J., & McFarlane, T. M. 1988, *MNRAS*, 231, 341
- Huang, C. D., Riess, A. G., Yuan, W., et al. 2019, arXiv e-prints, arXiv:1908.10883
- Hwang, H.-C., & Zakamska, N. 2019, arXiv e-prints, arXiv:1909.06375
- Inno, L., Bono, G., Matsunaga, N., et al. 2016, *ApJ*, 832, 176
- Iorio, G., & Belokurov, V. 2019, *MNRAS*, 482, 3868
- Iorio, G., Belokurov, V., Erkal, D., et al. 2018, *MNRAS*, 474, 2142
- Iwanek, P., Soszyński, I., Skowron, J., et al. 2019, *ApJ*, 879, 114
- Jayasinghe, T., Kochanek, C. S., Stanek, K. Z., et al. 2018, *MNRAS*, 477, 3145
- Jayasinghe, T., Stanek, K. Z., Kochanek, C. S., et al. 2019a, arXiv e-prints, arXiv:1911.09685
- . 2019b, *MNRAS*, 486, 1907
- . 2020a, *MNRAS*, 491, 13
- . 2020b, *MNRAS*, 493, 4186
- Jiang, D. 2020, *MNRAS*, 492, 2731
- Kodric, M., Riffeser, A., Hopp, U., et al. 2018, *AJ*, 156, 130
- Layden, A. C., Tiede, G. P., Chaboyer, B., Bunner, C., & Smitka, M. T. 2019, *AJ*, 158, 105
- Lebzelter, T., Trabucchi, M., Mowlavi, N., et al. 2019, *A&A*, 631, A24

- Lomb, N. R. 1976, *Ap&SS*, 39, 447
- Lutz, T. E., & Kelker, D. H. 1973, *PASP*, 85, 573
- Mahabal, A., Rebbapragada, U., Walters, R., et al. 2019, *PASP*, 131, 038002
- Martínez-Vázquez, C. E., Vivas, A. K., Gurevich, M., et al. 2019, *MNRAS*, 490, 2183
- Masci, F. J., Laher, R. R., Rusholme, B., et al. 2019, *PASP*, 131, 018003
- Matsunaga, N., Kawadu, T., Nishiyama, S., et al. 2011, *Nature*, 477, 188
- McNamara, D. H. 2011, *AJ*, 142, 110
- Medina, G. E., Muñoz, R. R., Vivas, A. K., et al. 2018, *ApJ*, 855, 43
- Minniti, D., Lucas, P. W., Emerson, J. P., et al. 2010, *NewA*, 15, 433
- Mowlavi, N., Lecoœur-Taïbi, I., Lebzelter, T., et al. 2018, *A&A*, 618, A58
- Muraveva, T., Delgado, H. E., Clementini, G., Sarro, L. M., & Garofalo, A. 2018, *MNRAS*, 481, 1195
- Neeley, J. R., Marengo, M., Freedman, W. L., et al. 2019, *MNRAS*, 2412
- Nelson, C. A., & Eggleton, P. P. 2001, *ApJ*, 552, 664
- Palaversa, L., Ivezić, Ž., Eyer, L., et al. 2013, *AJ*, 146, 101
- Palma, T., Minniti, D., Alonso-García, J., et al. 2019, *MNRAS*, 487, 3140
- Pietrukowicz, P., Dziembowski, W. A., Mróz, P., et al. 2013, *AcA*, 63, 379
- Pietrukowicz, P., Kozłowski, S., Skowron, J., et al. 2015, *ApJ*, 811, 113
- Pietrzyński, G., Graczyk, D., Gallenne, A., et al. 2019, *Nature*, 567, 200
- Pojmanski, G., Pilecki, B., & Szczygiel, D. 2005, *AcA*, 55, 275
- Ren, Y., Jiang, B.-W., Yang, M., & Gao, J. 2019, *ApJS*, 241, 35
- Riess, A. G., Casertano, S., Yuan, W., Macri, L. M., & Scolnic, D. 2019, *ApJ*, 876, 85
- Ripepi, V., Molinaro, R., Musella, I., et al. 2019, *A&A*, 625, A14
- Ripepi, V., Cioni, M.-R. L., Moretti, M. I., et al. 2017, *MNRAS*, 472, 808
- Rucinski, S. M. 2006, *MNRAS*, 368, 1319
- Scargle, J. D. 1982, *ApJ*, 263, 835
- Sesar, B., Hernitschek, N., Dierickx, M. I. P., Fardal, M. A., & Rix, H.-W. 2017, *ApJL*, 844, L4
- Skowron, D. M., Skowron, J., Mróz, P., et al. 2019a, *Science*, 365, 478
- . 2019b, *AcA*, 69, 305
- Snedden, C., Preston, G. W., Kollmeier, J. A., et al. 2018, *AJ*, 155, 45
- Soszynski, I., Poleski, R., Udalski, A., et al. 2008, *AcA*, 58, 163
- Soszyński, I., Udalski, A., Wrona, M., et al. 2019, *AcA*, 69, 321
- Stepien, K. 2006, *AcA*, 56, 199
- Strassmeier, K. G., Hall, D. S., Fekel, F. C., & Scheck, M. 1993, *A&AS*, 100, 173
- Stringer, K. M., Long, J. P., Macri, L. M., et al. 2019, *AJ*, 158, 16
- Thompson, T. A., Kochanek, C. S., Stanek, K. Z., et al. 2019, *Science*, 366, 637
- Trabucchi, M., Wood, P. R., Montalbán, J., et al. 2017, *ApJ*, 847, 139
- Udalski, A., Szymanski, M., Kaluzny, J., Kubiak, M., & Mateo, M. 1992, *AcA*, 42, 253
- Udalski, A., Szymański, M. K., & Szymański, G. 2015, *AcA*, 65, 1
- Udalski, A., Wyrzykowski, L., Pietrzynski, G., et al. 2001, *AcA*, 51, 221
- Udalski, A., Soszyński, I., Pietrukowicz, P., et al. 2018, *AcA*, 68, 315
- Wang, K., Deng, L., Zhang, X., et al. 2015, *AJ*, 150, 161
- Wang, S., & Chen, X. 2019, *ApJ*, 877, 116
- Wang, S., Chen, X., de Grijs, R., & Deng, L. 2018, *ApJ*, 852, 78
- Yakut, K., & Eggleton, P. P. 2005, *ApJ*, 629, 1055
- Yang, M., & Jiang, B. W. 2011, *ApJ*, 727, 53
- . 2012, *ApJ*, 754, 35
- Yang, M., Bonanos, A. Z., Jiang, B.-W., et al. 2018, *A&A*, 616, A175
- Yuan, W., Macri, L. M., He, S., et al. 2017, *AJ*, 154, 149
- Yuan, W., Macri, L. M., Javadi, A., Lin, Z., & Huang, J. Z. 2018, *AJ*, 156, 112
- Zhang, L.-Y., Pi, Q.-f., & Yang, Y.-G. 2014, *MNRAS*, 442, 2620
- Ziaali, E., Bedding, T. R., Murphy, S. J., Van Reeth, T., & Hey, D. R. 2019, *MNRAS*, 486, 4348